Realization of microwave amplification, attenuation, and frequency conversion using a single three-level superconducting quantum circuit

Yan-Jun Zhao,[1] Jiang-Hao Ding,[1] Z. H. Peng,[2] and Yu-xi Liu[1,3,*]

[1]*Institute of Microelectronics, Tsinghua University, Beijing 100084, China*
[2]*CEMS, RIKEN, Saitama 351-0198, Japan*
[3]*Tsinghua National Laboratory for Information Science and Technology (TNList), Beijing 100084, China*

(Dated: October 26, 2015)

Using different configurations of applied strong driving and weak probe fields, we find that only a single three-level superconducting quantum circuit (SQC) is enough to realize amplification, attenuation and frequency conversion of microwave fields. Such a three-level SQC has to possess Δ-type cyclic transitions. Different from the parametric amplification (attenuation) and frequency conversion in nonlinear optical media, the real energy levels of the three-level SQC are involved in the energy exchange when these processes are completed. We mainly show the efficiencies of the amplification and the frequency conversion for different types of driving fields. Our study provides a new method to amplify (attenuate) microwave, realize frequency conversion, and also lays a foundation for generating single or entangled microwave photon states using a single three-level SQC.

PACS numbers: 42.65.Es,42.65.Ky,75.30.Cr

arXiv:1510.05737v2 [quant-ph] 23 Oct 2015

I. INTRODUCTION

Three-wave mixing is very fundamental in nonlinear quantum optics [1]. It can be used to generate single photon or entangled photon pairs. Three-wave mixing can also be used to convert the frequency of the weak electromagnetic filed or amplify the weak electromagnetic signal by virtue of another strong driving field. In atomic systems with inversion symmetry, the three-wave mixing can only occur in a parametric way because of the selection rule in the electric-dipole interaction between the atoms and electric fields. Thus, the nonlinear interaction strength of the three-wave mixing is usually weak in the natural atomic systems. In contrast to the parametric weak nonlinearity realized by the virtual single- or two-photon processes, the nonlinear interaction strength can be increased significantly when the real energy exchange is involved. For example, in molecular systems [2–4], the inversion symmetry can be broken, and the transitions between any two energy levels are possible. In such cases, the three-wave mixing processing can be realized using real energy transitions between energy levels. In artificial atoms, e.g., semiconducting quantum dots or superconducting quantum circuits (SQCs), the inversion symmetry of their potential energy can be artificially controlled by externally applied field, that is, the selection rule of the artificial atoms can be engineered. Thus, they provide us a new platform to manipulate and engineer linear and nonlinear quantum processes. For example,the single photon strong coupling can be achieved between microwave and mechanical modes using a superconducting flux qubit [5]. It is also possible to realize three-wave mixing using real energy transitions between energy levels of a single SQC [6].

The SQCs [7–13] are extensively explored for the realization of qubits which are basic building blocks of quantum information processing. These superconducting artificial atoms can also be used not only to demonstrate phenomena occurred in atomic physics and quantum optics, but also to show some novel results, which cannot be found in natural atomic systems. For example, the dressed states [14, 15] have been experimentally demonstrated using superconducting charge qubit circuits [16, 17]. The Autler-Townes splitting [18–24] and coherent population trapping [25] have also been observed in three-level SQCs. Experimentalists are trying to find a way to realize the electromagnetically induced transparency in varieties of three-level SQDs [26–30]. Moreover, the coexistence of single- and two-photon processes [31] in three-level superconducting flux qubit circuits [31, 32] has been experimentally demonstrated [33] by designed circuit QED systems. However, such phenomenon cannot be demonstrated using three-level natural atoms because of the electric-dipole transition rule.

The microwave amplification has been experimentally demonstrated by a single three-level artificial atom in open one-dimensional space [34], a dressed [35] or a doubly-dressed superconducting flux [36] qubit circuit. The coherent frequency conversion has be demonstrated using two internal degrees of freedom of a single dc-SQUID phase qubit circuit [37]. The parametric down conversion and squeezing of two-mode quantized microwave fields using circuit QED are theoretically studied [38]. Moreover, the parametric three-wave mixing devices have also been experimentally demonstrated [39, 40]. It was shown that the amplifiers with single artificial atoms [34] are different from the Josephson junction based parametric three-wave mixing devices [39, 40] or amplifiers [41–44]. A main difference is that the real energy exchange between discrete energy levels is involved when the single artificial atom amplifiers are implemented. We recently showed that a three-level flux qubit circuits [6] with Δ-type cyclic transitions can be used to generate three-wave mixing.

Motivated by the work [6, 34], we now give a detailed study on the microwave amplification and frequency conversion by a single three-level SQC with Δ-type transitions, which can

*Electronic address: yuxiliu@mail.tsinghua.edu.cn

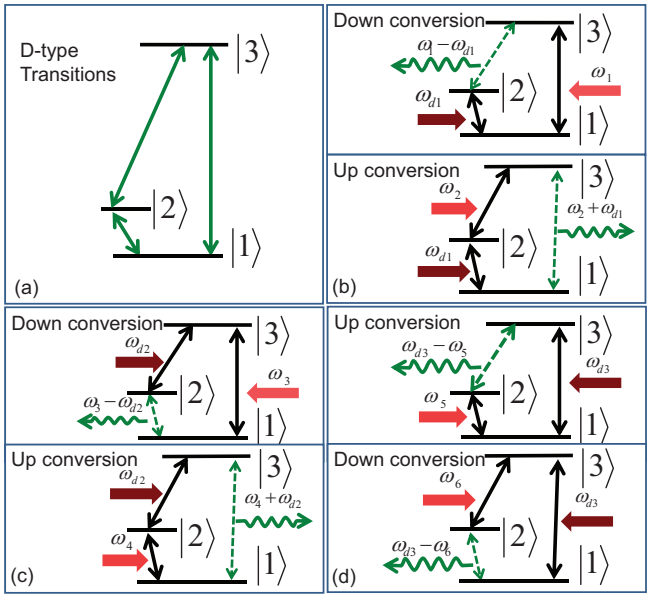

FIG. 1: Schematic diagrams for three-level superconducting quantum circuits with the Δ-type transitions in (a). The driving field has three different ways to be applied for microwave frequency conversion or amplification processes as shown in (b), (c) and (d). Each of three figures includes two panels, corresponding to up and down frequency conversions, respectively. In all the three figures, the light red arrows mean the signal field. However, the dark red arrows mean the strong driving field. The green arrows denote the converted signal.

be realized by superconducting flux [31, 32], phase [45–47], or Xmon qubit circuits [48]. For the concreteness, we here focus on flux qubit circuits. In our study, we mainly study the conversion efficiency and the gain and attenuation of the weak signal field. Our paper is organized as follows. In Sec. II, we describe the model Hamiltonian, the master equations, and the basic calculation method. In Sec. III, taking what we call driving type (1) as an example, we give detailed studies on the microwave attenuation and frequency conversion. In Sec. IV, we will give main results on the microwave amplification, attenuation and frequency conversion for what we call driving type (3). In Sec. V, we will discuss the measurements and experimental feasibilities and summarize our results. We mention that the study on the microwave amplification (attenuation) and frequency conversion for driving type (2) is given in Appendix B.

II. THEORETICAL MODEL AND CALCULATION METHOD

We study microwave amplifications, attenuation and frequency conversions in a three-level superconducting artificial atom with Δ-type transitions [31], as schematically shown in Fig. 1(a). The three energy levels are denoted by $|1\rangle$, $|2\rangle$, and $|3\rangle$. Here, we specify our study to superconducting flux qubit circuits, consisting of three Josephson junctions [31, 32]. We assume that the bias magnetic flux is not at the optimal point so that the three energy levels chosen from such circuit can possess Δ-type transition when the external fields are applied. We also assume that the three-level system is placed inside an open one-dimensional transmission line resonator as in Ref. [34]. Hereafter, for simplicity, we use three-level systems to denote such three-level superconducting flux qubit circuits.

A. Hamiltonian

To realize the microwave amplification, attenuation, or frequency conversion, a strong driving field has to be applied to the three-level system with Δ-type transitions, as shown in Figs. 1(b), (c) and (d), the strong driving field can be applied to couple: (1) the energy levels $|1\rangle$ and $|2\rangle$; or (2) the energy levels $|2\rangle$ and $|3\rangle$; or (3) the energy levels $|1\rangle$ and $|3\rangle$. Corresponding to each configuration of the driving filed, the signal field can be applied in two ways. For example, as shown in two panels of Fig. 1(b), the signal field can be applied to either the energy levels $|1\rangle$ and $|3\rangle$ (shown in up panel of Fig. 1(b)), or the energy levels $|2\rangle$ and $|3\rangle$ (shown in down panel of Fig. 1(b)) when the driving field is applied to the energy levels $|1\rangle$ and $|2\rangle$.

In strong driving types (1) and (2) as shown in Figs. 1(b) and (c), the frequency down or up conversion can be realized by properly applying the signal field. But in the driving type (3) as shown in Fig. 1(d), the up and down conversions are a little bit different from the types (1) and (2). In the types (1) and (2), the down (up) frequency conversion is the difference between (sum of) frequencies of the signal and driving fields. However, in the type (3), both the down and up frequency conversions are the difference between the frequencies of signal and driving fields, when the frequency difference is larger than the signal frequency, we call this process as the up conversion, otherwise the down conversion.

In all three driving ways with applied signal fields, the Hamiltonian can be generally given by

$$H^{(l)} = \hbar\omega_{21}\sigma_{22} + \hbar\omega_{31}\sigma_{33} + H_R^{(l)}(t) + H_\varepsilon^{(l)}(t) + H_T^{(l)}(t), \quad (1)$$

from Ref. [6] when one of the weak fields is replaced by a strong field. We note that we sometimes also call signal fields as probing fields. Hereafter, $\sigma_{mn} = |m\rangle\langle n|$ with n, $m = 1, 2,$ or 3. The superscript $l = 1, 2,$ or 3 is used to represent different driving types. In the type of the lth driving, the symbol $H_R^{(l)}(t)$ (or $H_\varepsilon^{(l)}(t)$) denotes the interaction Hamiltonian between the strong driving field (or the weak signal field) and the three-level system, however, the symbol $H_T^{(l)}(t)$ describes the interaction Hamiltonian between the three-level system and environment in open one-dimensional transmission line, and can be related to practical experimental parameters, using the model as in Refs. [49, 50]. Hereafter, we call strong driving and weak signal fields as driving and signal fields.

All types of the interaction Hamiltonians $H_R^{(l)}(t)$ and $H_\varepsilon^{(l)}(t)$ have been summarized in Table I. For convenience

TABLE I: Summary of the interaction Hamiltonian $H_R^{(l)}(t)$ between the three-level superconducting artificial atoms and the strong driving field, which can be applied to the three-level systems in three different ways. Corresponding to each strong driving field, the probe fields can be applied to the three-level system in two different ways with two different interaction Hamiltonians $H_{1\varepsilon}^{(l)}(t)$ and $H_{2\varepsilon}^{(l)}(t)$. Here, $\hbar\Omega_{mn,l} = -MI_{mn}\tilde{I}_{dl}(0)/2$ and $\hbar\varepsilon_{mn,k} = -MI_{mn}\tilde{I}_{pk}(0)/2$. The incident driving current is assumed as $I_{dl}(x,t) = \mathrm{Re}[\tilde{I}_{dl}(x)e^{-i\omega_{dl}t}]$ where $l = 1, 2$,or 3, and x is the position coordinate. The incident signal currents are assumed as $I_{pk}(x,t) = \mathrm{Re}[\tilde{I}_{pk}(x)e^{-i\omega_k t}]$ with $k = 1$ or $k = 2$. The parameters I_{mn} are loop current matrix of the three-level system.

Type of driving field	Interaction Hamiltonian with the strong driving field	Interaction Hamiltonian with the probe field
Type (1)	$H_R^{(1)}(t) = \hbar[\Omega_{21,1}\sigma_{21}\exp(-i\omega_{d1}t) + \text{H.c.}]$	$H_{1\varepsilon}^{(1)}(t) = \hbar[\varepsilon_{31,1}\sigma_{31}\exp(-i\omega_1 t) + \text{H.c.}]$ $H_{2\varepsilon}^{(1)}(t) = \hbar[\varepsilon_{32,2}\sigma_{32}\exp(-i\omega_2 t) + \text{H.c.}]$
Type (2)	$H_R^{(2)}(t) = \hbar[\Omega_{32,2}\sigma_{32}\exp(-i\omega_{d2}t) + \text{H.c.}]$	$H_{1\varepsilon}^{(2)}(t) = \hbar[\varepsilon_{31,3}\sigma_{31}\exp(-i\omega_3 t) + \text{H.c.}]$ $H_{2\varepsilon}^{(2)}(t) = \hbar[\varepsilon_{32,4}\sigma_{32}\exp(-i\omega_4 t) + \text{H.c.}]$
Type (3)	$H_R^{(3)}(t) = \hbar[\Omega_{31,3}\sigma_{31}\exp(-i\omega_{d3}t) + \text{H.c.}]$	$H_{1\varepsilon}^{(3)}(t) = \hbar[\varepsilon_{21,5}\sigma_{21}\exp(-i\omega_5 t) + \text{H.c.}]$ $H_{2\varepsilon}^{(3)}(t) = \hbar[\varepsilon_{32,6}\sigma_{32}\exp(-i\omega_6 t) + \text{H.c.}]$

of following discussions, below we first use the driving type (1) as an example to give detailed derivations. In the driving type (1), the Hamiltonian $H_R^{(1)}(t)$ can be given as

$$H_R^{(1)}(t) = \hbar[\Omega_{21,1}\sigma_{21}\exp(-i\omega_{d1}t) + \text{H.c.}]. \quad (2)$$

with $\Omega_{21,1} = -MI_{21}\tilde{I}_{d1}(0)/2$. Here M is the mutual inductance, and I_{21} is the matrix element of the persistent current in the loop of three-level superconducting flux qubit circuit. The incident driving current is assumed as $I_{d1}(x,t) = \mathrm{Re}[\tilde{I}_{d1}(x)e^{-i\omega_{d1}t}]$. We assume that the three-level system is placed at the position of $x = 0$ and also $\Omega_{21,1}$ is a real number without loss of generality.

Corresponding to the Hamiltonian in Eq. (2), the Hamiltonian $H_\varepsilon(t)$ has two different types, described by $H_{1\varepsilon}(t)$ or $H_{2\varepsilon}(t)$. The Hamiltonian $H_{1\varepsilon}(t)$ can be written as

$$H_{1\varepsilon}^{(1)}(t) = \hbar[\varepsilon_{31,1}\sigma_{31}\exp(-i\omega_1 t) + \text{H.c.}], \quad (3)$$

for that the signal field is applied to the energy levels $|1\rangle$ and $|3\rangle$. The Hamiltonian in Eq. (1) with $H_R^{(1)}(t)$ in Eq. (2) and $H_{1\varepsilon}^{(1)}(t)$ in Eq. (3) describes the frequency down conversion as shown in the up panel of Fig. 1(b). However, the Hamiltonian $H_{2\varepsilon}(t)$ can be written as

$$H_{2\varepsilon}^{(1)}(t) = \hbar[\varepsilon_{32,2}\sigma_{32}\exp(-i\omega_2 t) + \text{H.c.}], \quad (4)$$

for that the signal filed is applied to the energy levels $|2\rangle$ and $|3\rangle$. That is, the Hamiltonian in Eq. (1) with $H_R^{(1)}(t)$ in Eq. (2) and $H_{2\varepsilon}^{(1)}(t)$ in Eq. (4) describes the frequency up conversion as shown in the down panel of Fig. 1(b). The coupling strengths between the weak signal field and three-level system are given as $\hbar\varepsilon_{31,1} = -MI_{31}\tilde{I}_{p1}(0)/2$ and $\hbar\varepsilon_{32,2} = -MI_{32}\tilde{I}_{p2}(0)/2$, respectively. The parameters I_{31} and I_{32} are loop current matrix of the three-level system. The incident signal currents are assumed as $I_{pk}(x,t) = \mathrm{Re}[\tilde{I}_{pk}(x)e^{-i\omega_k t}]$ with $k = 1$ or $k = 2$.

For all driving types, we assume that the strength of the Rabi frequency $\Omega_{mn,l}$ for the driving field is much bigger than the strength of the Rabi frequency $\varepsilon_{m'n',k'}$ for the weak signal field, i.e., $|\Omega_{mn,l}| \gg |\varepsilon_{m'n',k'}|$. The driving strength $\Omega_{mn,l}$ is assumed real as well. To conveniently treat the amplification and frequency conversions for given driving field, we use

$$H_\varepsilon^{(l)}(t) = H_{1\varepsilon}^{(l)}(t) + H_{2\varepsilon}^{(l)}(t) \quad (5)$$

to unify the following calculations for different types of the probe fields.

B. Calculation method and master equation

For all three types of driving fields, the frequency conversion and the amplification of the signal field can be studied via the master equation of the reduced density matrix P of the system

$$\frac{\partial P}{\partial t} = \frac{1}{i\hbar}[H_{\text{eff}}^{(l)}, P] + \mathcal{L}[P], \quad (6)$$

where P will be replaced in the following calculations by

$$P \equiv \begin{cases} \rho, & l = 1 \\ \chi, & l = 2 \\ s, & l = 3 \end{cases} \quad (7)$$

to distinguish the reduced density matrix of the system in three different driving types. Here, $H_{\text{eff}}^{(l)}$ denotes the effective Hamiltonian of the three-level system of the lth driving type in the rotating reference frame. The dissipation of the

system is described via

$$\mathcal{L}[P] = \sum_m \left(\sum_{k>m} \gamma_{km} P_{kk} - \sum_{k<m} \gamma_{mk} P_{mm} \right) \sigma_{mm} - \sum_{m \neq n} \frac{1}{2} \Gamma_{mn} P_{mn} \sigma_{mn}. \quad (8)$$

Here, $P_{mn} \equiv P_{mn}(t)$ are matrix elements of the reduced density operator $P(t)$. The dynamics of the system can be given by solving equations of motion

$$\frac{\partial P_{mn}}{\partial t} = \frac{1}{i\hbar} \left[H_{\text{eff}}^{(l)}, P \right]_{mn} - \frac{1}{2} \Gamma_{mn} P_{mn}, m > n \quad (9)$$

$$\frac{\partial P_{11}}{\partial t} = \frac{1}{i\hbar} \left[H_{\text{eff}}^{(l)}, P \right]_{11} + \gamma_{21} P_{22} + \gamma_{31} P_{33}, \quad (10)$$

$$\frac{\partial P_{22}}{\partial t} = \frac{1}{i\hbar} \left[H_{\text{eff}}^{(l)}, P \right]_{22} + \gamma_{32} P_{33} - \gamma_{21} P_{22}, \quad (11)$$

$$\frac{\partial P_{33}}{\partial t} = \frac{1}{i\hbar} \left[H_{\text{eff}}^{(l)}, P \right]_{33} - (\gamma_{31} + \gamma_{32}) P_{33}, \quad (12)$$

for reduced density matrix elements in Eq. (6) with $\Gamma_{21} = \gamma_{21} + \gamma_{21}^{\phi}$, $\Gamma_{31} = \gamma_{31} + \gamma_{32} + \gamma_{31}^{\phi}$, and $\Gamma_{32} = \gamma_{31} + \gamma_{32} + \gamma_{21} + \gamma_{32}^{\phi}$. The decay and dephasing rates γ_{mn}, γ_{mn}^{ϕ} between energy levels $|m\rangle$ and $|n\rangle$ of the three-level system are related to the supercurrent through the superconducting loop [30] and can be given as (the detailed derivation can be found in Appendix A):

$$\gamma_{mn} = \frac{|MI_{mn}|^2 \hbar \omega_{mn}}{\hbar^2 Z_T}, m > n, \quad (13)$$

$$\gamma_{mn}^{\phi} = \frac{M^2 k_B T}{\hbar^2 Z_T} (I_{mm} - I_{nn})^2, m > n, \quad (14)$$

where k_B, T and Z_T represent the Boltzmann constant, the environmental temperature, and the characteristic impendence of the transmission line. The transition frequencies between any two energy levels and decay rates of the three-level system are plotted in Fig. 2 using the basic model (e.g., in Ref. [31]) of the three-junction superconducting flux qubit circuit. The Josephson energy E_J, charge energy E_C, and the area ratio α between the small and large junction refer to Ref. [6]. The mutual inductance M and sample temperature T are referred to Ref. [58] and Ref. [57], respectively. For concreteness of the discussions, hereafter the parameters for numerical calculations are taken from Fig. 2. However, our derivation can also be applied to other sets of parameters.

It is not easy to obtain the exact solutions of the nonlinear equations in Eqs. (9-12), because the steady state response contains infinite components of different frequencies in nonlinear systems. Thus, as extensively used method in nonlinear optics [1], we now seek the solutions of Eq. (6) in the form of a power series expansion in the strengths $\varepsilon_{mn,k}$, that is, a solution of the form

$$P(t) = P^{(0)} + P^{(1)}(t) + \cdots + P^{(r)}(t) + \cdots, \quad (15)$$

for the reduced density matrix P of the three-level system. Here, $P^{(0)}$ is the steady state solution when the signal field is not applied to the system, however the rth-order reduced density matrix $P^{(r)}(t)$ is proportional to the products $\varepsilon_{mn,k}^{p} \varepsilon_{m'n'k'}^{q}$ ($m \neq n$ and $m' \neq n'$) of the amplitudes for signal fields with $r = p + q$. That is, our solution is exact in the amplitude of the Rabi frequency $\Omega_{pq,l}$ of the driving field and is correct to the lowest order in the amplitudes $\varepsilon_{mn,k}$ of the signal fields.

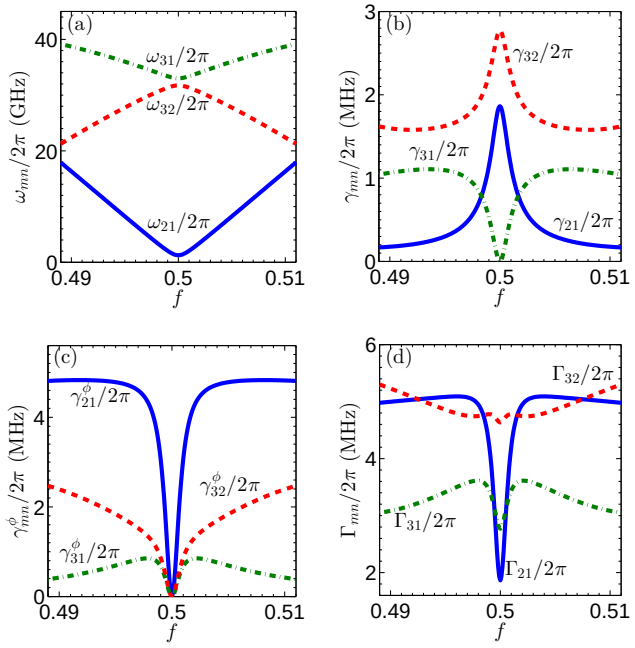

FIG. 2: Energy gaps $\omega_{21}/2\pi$ (solid blue), $\omega_{31}/2\pi$ (dash-dotted green), and $\omega_{32}/2\pi$ (dashed red) have been plotted as functions of the reduced magnetic flux bias f in (a). Bias-dependent relaxation rates $\gamma_{21}/2\pi$ (solid blue), $\gamma_{31}/2\pi$ (dash-dotted green), and $\gamma_{32}/2\pi$ (dashed red) have been plotted in (b). Bias-dependent pure dephasing rates $\gamma_{21}^{\phi}/2\pi$ (solid blue), $\gamma_{31}^{\phi}/2\pi$ (dash-dotted green), and $\gamma_{32}^{\phi}/2\pi$ (dashed red) have been plotted in (c). Bias-dependent total dephasing rates $\Gamma_{21}/2\pi$ (solid blue), $\Gamma_{31}/2\pi$ (dash-dotted green), and $\Gamma_{32}/2\pi$ (dashed red) have been plotted in (d). The parameters are given by $E_J/E_C = 48$, $E_J = 192\,\text{GHz} \times h$, $\alpha = 0.8$, $M = 10.7\,\text{pH}$, $T = 40\,\text{mK}$, and $Z_T = 50\,\Omega$, with h being the Plank constant.

C. Transmitted current

The frequency conversion and amplification can be measured through the transmitted current signal $I_{tl}(x,t)$ where l also refers to the driving type. Using the input-output theory extensively discussed in Refs. [50–54], the transmitted current at $x = 0$ can be given by

$$I_{tl}(0,t) = I_{dl}(0,t) + \sum_{k=2l-1}^{2l} I_{pk}(0,t) + I_{sl}(0,t), \quad (16)$$

for the driving type (l). Here $I_{sl}(x,t)$ is the scattered current signal and

$$I_{sl}(0,t)=\sum_{3\geq m>n\geq 1}\mathrm{Re}\left[\frac{i\hbar\gamma_{mn}}{MI_{mn}}P_{E,mn}(t)\right]. \quad (17)$$

Here, $P_E\equiv P_E(t)$ is the reduced the density operator in the coordinate system of the experimental laboratory, and $P_{E,mn}$ is its matrix element. That is, $P_E(t)$ can be obtained from $P(t)$ in the rotating reference frame through $P_E(t)=U_l^{\dagger}(t)P(t)U_l(t)$, where $U_l(t)$ can be specified for different driving types below. To examine the frequencies of the output signal, we expand $P_{E,mn}(t)$ in the frequency domain as

$$P_{E,mn}(t)=\sum_{\omega}\tilde{P}_{E,mn}(\omega)\,e^{-i\omega t}. \quad (18)$$

Then for the scattered signal, we have

$$I_{sl}(0,t)=\sum_{\omega}\mathrm{Re}\left\{\tilde{I}_{sl}(0,\omega)\,e^{-i\omega t}\right\}, \quad (19)$$

where

$$\tilde{I}_{sl}(0,\omega)=\sum_{m>n}\frac{i\hbar\gamma_{mn}}{MI_{mn}}\tilde{P}_{E,mn}(\omega) \quad (20)$$

represents the amplitude of the scattered signal at the frequency ω.

III. MICROWAVE ATTENUATION AND FREQUENCY CONVERSIONS FOR DRIVING TYPE (1)

A. Solutions

We first use the driving type (1) as an example to study the amplification and the frequency conversions. In the rotating reference frame with the unitary transform $U_1=\exp(-i\omega_{d1}\sigma_{22}t)$, the effective Hamiltonian $H_{\rm eff}^{(1)}$ of the driving type (1) can be written as

$$\begin{aligned}H_{\rm eff}^{(1)}=&\hbar\Delta_{21,1}\,\sigma_{22}+\hbar\omega_{31}\sigma_{33}+\hbar(\Omega_{21,1}\sigma_{21}+\text{H.c.}) \quad (21)\\ &+\hbar\left[\varepsilon_{31,1}\,\sigma_{31}e^{-i\omega_1 t}+\varepsilon_{32,2}\,\sigma_{32}e^{-i\omega_{2+}t}+\text{H.c.}\right],\end{aligned}$$

with $\Delta_{21,1}=\omega_{21}-\omega_{d1}$ and $\omega_{2+}=\omega_2+\omega_{d1}$. Hereafter, $\Delta_{21,1}$ is called the driving detuning. Using Eq. (15) and replacing $H_{\rm eff}^{(l)}$ in Eq. (6) by $H_{\rm eff}^{(1)}$ in Eq. (21), we can derive a master equation for the rth-order reduced density matrix as

$$\begin{aligned}\dot{\rho}^{(r)}=&-i\left[\Delta_{21,1}\,\sigma_{22}+\omega_{31}\sigma_{33}+(\Omega_{21,1}\sigma_{21}+\text{H.c.}),\rho^{(r)}\right]\\ &+\mathcal{L}\rho^{(r)}-i\left[\varepsilon_{31,1}\,\sigma_{31}\exp(-i\omega_1 t)+\text{H.c.},\rho^{(r-1)}\right]\\ &-i\left[\varepsilon_{32,2}\,\sigma_{32}\exp(-i\omega_{2+}t)+\text{H.c.},\rho^{(r-1)}\right]. \quad (22)\end{aligned}$$

We are only interested in the response of the driven three-level system to the weak signal field. Thus, we first obtain the steady-state solutions using equation

$$\begin{aligned}\dot{\rho}^{(0)}=&-i\left[\Delta_{21,1}\,\sigma_{22}+\omega_{31}\sigma_{33}+(\Omega_{21,1}\sigma_{21}+\text{H.c.}),\rho^{(0)}\right]\\ &+\mathcal{L}\rho^{(0)}, \quad (23)\end{aligned}$$

for $r=0$ in Eq. (22) when the signal field is not applied. From Eq. (23), we can obtain equations of motion for all matrix elements $\rho_{mn}^{(0)}$. By setting $\partial\rho_{mn}^{(0)}/\partial t=0$, all nonzero density matrix elements in the steady state are given by

$$\rho_{11}^{(0)}=\frac{1}{A}\left(\gamma_{21}\Gamma_{21}^2+4\Gamma_{21}\Omega_{21,1}^2+4\gamma_{21}\Delta_{21,1}^2\right), \quad (24)$$

$$\rho_{22}^{(0)}=1-\rho_{11}^{(0)}, \quad (25)$$

$$\rho_{12}^{(0)}=\rho_{21}^{(0)*}=\frac{i\Omega_{21,1}\gamma_{21}}{A}\left(2\Gamma_{21}+i4\Delta_{21,1}\right), \quad (26)$$

with the parameter $A=\gamma_{21}\Gamma_{21}^2+8\Gamma_{21}\Omega_{21,1}^2+4\gamma_{21}\Delta_{21,1}^2$. Based on the zeroth order solution, we can easily obtain equations of motion for the reduced density matrix $\rho^{(1)}$ in the first order approximation. Because equations of motion for the density matrix $\rho^{(1)}$ have two different frequencies, thus we expand the density matrix elements $\rho_{mn}^{(1)}$ of $\rho^{(1)}$ in the frequency domain as

$$\rho_{mn}^{(1)}(t)=\tilde{\rho}_{mn}^{(1)}(\omega_1)\,e^{-i\omega_1 t}+\tilde{\rho}_{mn}^{(1)}(\omega_{2+})\,e^{-i\omega_{2+}t}, \quad (27)$$

where $m>n$. Using Eq. (27) and also equations of motion of reduced density matrix elements $\rho_{mn}^{(1)}(t)$, we obtain the zero matrix elements

$$\rho_{11}^{(1)}(t)=\rho_{22}^{(1)}(t)=\rho_{33}^{(1)}(t)=\rho_{12}^{(1)}(t)=\rho_{21}^{(1)}(t)=0. \quad (28)$$

and nonzero matrix elements

$$\tilde{\rho}_{31}^{(1)}(\omega_{2+})=-i\frac{\varepsilon_{32,2}}{B}\left[B_1\rho_{21}^{(0)}+i\Omega_{21,1}\rho_{22}^{(0)}\right], \quad (29)$$

$$\tilde{\rho}_{32}^{(1)}(\omega_{2+})=-\frac{i\varepsilon_{32,2}}{B}\left[B_2\rho_{22}^{(0)}+i\Omega_{21,1}\rho_{21}^{(0)}\right], \quad (30)$$

$$\tilde{\rho}_{31}^{(1)}(\omega_1)=-i\frac{\varepsilon_{31,1}}{C}\left[C_2\rho_{11}^{(0)}+i\Omega_{21,1}\rho_{12}^{(0)}\right], \quad (31)$$

$$\tilde{\rho}_{32}^{(1)}(\omega_1)=-i\frac{\varepsilon_{31,1}}{C}\left[C_1\rho_{12}^{(0)}+i\Omega_{21,1}\rho_{11}^{(0)}\right], \quad (32)$$

where the parameters are given by $B=B_1B_2+\Omega_{21,1}^2$ and $C=C_1C_2+\Omega_{21,1}^2$ with

$$B_1=i\delta_{32,2}+\frac{\Gamma_{32}}{2},\quad B_2=i\Delta_{21,1}+i\delta_{32,2}+\frac{\Gamma_{31}}{2}, \quad (33)$$

$$C_1=i\delta_{31,1}+\frac{\Gamma_{31}}{2},\quad C_2=-i\Delta_{21,1}+i\delta_{31,1}+\frac{\Gamma_{32}}{2}. \quad (34)$$

The detunings are given by $\delta_{32,2}=\omega_{32}-\omega_2$ and $\delta_{31,1}=\omega_{31}-\omega_1$. Therefore, in the time domain, the density matrix elements $\rho_{31}^{(1)}(t)$ and $\rho_{32}^{(1)}(t)$ can be given as

$$\rho_{31}^{(1)}(t)=\tilde{\rho}_{31}^{(1)}(\omega_{2+})e^{-i\omega_{2+}t}+\tilde{\rho}_{31}^{(1)}(\omega_1)e^{-i\omega_1 t}, \quad (35)$$

$$\rho_{32}^{(1)}(t)=\tilde{\rho}_{32}^{(1)}(\omega_{2+})e^{-i\omega_{2+}t}+\tilde{\rho}_{32}^{(1)}(\omega_1)e^{-i\omega_1 t}. \quad (36)$$

It is clear that the density matrix elements $\rho_{13}^{(1)}(t)$ and $\rho_{23}^{(1)}(t)$ can be obtain by taking complex conjugate of $\rho_{31}^{(1)}(t)$ and $\rho_{32}^{(1)}(t)$, respectively. We now go back to the coordinate system of the experimental laboratory with the reverse unitary transform $U_1 = \exp(i\omega_{d1}\sigma_{22}t)$, and then we have

$$\rho_{E,31}^{(1)}(t) = \tilde{\rho}_{31}^{(1)}(\omega_{2+})e^{-i\omega_{2+}t} + \tilde{\rho}_{31}^{(1)}(\omega_1)e^{-i\omega_1 t}, \quad (37)$$

$$\rho_{E,32}^{(1)}(t) = \tilde{\rho}_{32}^{(1)}(\omega_{2+})e^{-i\omega_{2}t} + \tilde{\rho}_{32}^{(1)}(\omega_{1-})e^{-i\omega_{1-} t}, \quad (38)$$

with $\omega_{1-} = \omega_1 - \omega_{d1}$.

It is clear that the components with the frequencies ω_1 and ω_2 correspond to the amplification or absorption for the weak probe fields. However, the components with the frequencies $\omega_{1-} = \omega_1 - \omega_{d1}$ and $\omega_{2+} = \omega_2 + \omega_{d1}$ correspond to the frequency down and up conversions, respectively. As explained by the quantum input-output theory [50–54], the output field carries the system's information after the interaction between the input noise and the system. Therefore, we will study the output field of the different components in Eqs. (37) and (38).

B. Efficiencies of frequency down and up conversions

Based on the calculation via the first order perturbation theory, we can obtain the scattered current with either the frequency ω_{1-} or the frequency ω_{2+},

$$\tilde{I}_{s1}(0,\omega) = \sum_{m>n} \frac{i\hbar\gamma_{mn}}{MI_{mn}} \tilde{\rho}_{E,mn}(\omega), \quad (39)$$

with $\omega = \omega_{1-}$ or $\omega = \omega_{2+}$, which corresponds to either the frequency down or the frequency up conversion. Using Eq. (38) and Eq. (32), we can obtain

$$\tilde{I}_{s1}(0,\omega_{1-}) = \frac{i\hbar\gamma_{32}}{MI_{32}} \tilde{\rho}_{E,32}(\omega_{1-}) = \frac{i\hbar\gamma_{32}}{MI_{32}} \tilde{\rho}_{32}^{(1)}(\omega_1). \quad (40)$$

We define the down conversion efficiency as the ratio between the generated current intensity of new frequency ω_{1-} and the incident signal current intensity of the original frequency ω_1

$$\eta_1 = \frac{\tilde{I}_{s1}(0,\omega_{1-})}{\tilde{I}_{p1}(0)} = \frac{-I_{31}\gamma_{32}}{2I_{32}C}\left[C_1\rho_{12}^{(0)} + i\Omega_{21,1}\rho_{11}^{(0)}\right]. \quad (41)$$

Similarly, using Eqs. (38) and (29), we have

$$\tilde{I}_{s1}(0,\omega_{2+}) = \frac{i\hbar\gamma_{31}}{MI_{31}} \tilde{\rho}_{E,31}(\omega_{2+}) = \frac{i\hbar\gamma_{31}}{MI_{31}} \tilde{\rho}_{31}^{(1)}(\omega_{2+}). \quad (42)$$

Then the up conversion efficiency can be given by

$$\eta_2 = \frac{\tilde{I}_{s1}(0,\omega_{2+})}{\tilde{I}_{p2}(0)} = \frac{-I_{32}\gamma_{31}}{2I_{31}B}\left[B_1\rho_{21}^{(0)} + i\Omega_{21,1}\rho_{22}^{(0)}\right]. \quad (43)$$

C. Attenuation rates of incident signal fields

The incident signal fields can be either amplified or attenuated, depending on the driving type. In the driving type (1), the frequency conversion process will take energy away from the signal field, thus the signal field is attenuated, not amplified.

The scattered current corresponding to the the frequency ω_1 or ω_2 of the incident signal field can be given by

$$\tilde{I}_{s1}(0,\omega) = \sum_{m>n} \frac{i\hbar\gamma_{mn}}{MI_{mn}} \tilde{\rho}_{E,mn}(\omega), \quad (44)$$

with $\omega = \omega_1$ or the frequency $\omega = \omega_2$ when the incident signal field is not considered. Using Eqs. (31), (37) and (38), we have

$$\tilde{I}_{s1}(0,\omega_1) = \frac{i\hbar\gamma_{31}}{MI_{31}} \tilde{\rho}_{E,31}(\omega_1) = \frac{i\hbar\gamma_{31}}{MI_{31}} \tilde{\rho}_{31}^{(1)}(\omega_1) \quad (45)$$

corresponding to scattered current with the frequency ω_1. Thus the total current would be summation of the incident signal current and the scattered current with the same frequency. We hereby define the attenuation rate G_1, for convenience, to term the ratio between the total transmitted signal current and the incident one

$$G_1 = 1 + R_1, \quad (46)$$

with

$$R_1 = \frac{\tilde{I}_{s1}(0,\omega_1)}{\tilde{I}_{p1}(0)} = -\frac{\gamma_{31}}{2C}\left[C_2\rho_{11}^{(0)} + i\Omega_{21,1}\rho_{12}^{(0)}\right], \quad (47)$$

which is called the reflection coefficient by us. The parameter G_1 can be used to study the properties of the output field corresponding to the signal frequency ω_1.

Similarly, using Eqs. (30), (37) and (38), we can also obtain the scattered current corresponding to the frequency ω_2 as

$$\tilde{I}_{s1}(0,\omega_2) = \frac{i\hbar\gamma_{32}}{MI_{32}} \tilde{\rho}_{E,32}(\omega_2) = \frac{i\hbar\gamma_{32}}{MI_{32}} \tilde{\rho}_{32}^{(1)}(\omega_{2+}). \quad (48)$$

The attenuation rate G_2 is given by

$$G_2 = 1 + R_2, \quad (49)$$

where

$$R_2 = \frac{\tilde{I}_{s1}(0,\omega_2)}{\tilde{I}_{p2}(0)} = -\frac{\gamma_{32}}{2B}\left[B_2\rho_{22}^{(0)} + i\Omega_{21,1}\rho_{21}^{(0)}\right], \quad (50)$$

is the corresponding reflection coefficient. The parameter G_2 can be used to study the properties of the output field corresponding to the signal frequency ω_2.

Here, we emphasize that $|G_k| < 1$, because the signal is attenuated. Thus when $|G_k|$ takes the minimum value, it means the attenuation is maximum.

D. Discussions and numerical calculations

We summarize the parameters that determine the gains G_k and the conversion efficiencies η_k with $k = 1, 2$. From Eqs. (41), (43), (46) and (49), we know that G_k and η_k are

mainly determined by the driving strength $\Omega_{21,1}$, the driving (signal) detunings between the driving field (signal field) and the three-level system, and the decay rates (e.g., γ_{mn} and Γ_{mn}). The decay rates actually depend on the reduced magnetic flux bias f as shown in Figs. 2(b) and (d). Thus, the generic parameters that determine G_k and η_k are $\Delta_{21,1}$, $\Omega_{21,1}$ and f, as well as $\delta_{31,1}$ for $k=1$, or $\delta_{32,2}$ for $k=2$. Because there is only attenuation of the incident signal field in the driving type (1), the minimum value of G_k corresponds to the minimum attenuation. Thus the maximum η_k and minimum G_k are studied as follows.

1. *Microwave frequency conversion and attenuation with variations of the driving detuning*

We now study how the maximum frequency conversion efficiencies and minimum attenuation can be obtained by changing the driving detuning $\Delta_{21,1}$ when other parameters are given. We know that the extreme values of η_1 and G_1 correspond to the poles

$$\delta_{31,1}^{(\pm)} = \frac{1}{2}\left(\Delta_{21,1} + i\frac{\Gamma_{31}+\Gamma_{32}}{2}\right) \pm \frac{1}{2}\Delta_{21} \equiv \delta_{31}^{(\pm)}\left(\Delta_{21,1}\right) \tag{51}$$

of η_1, which is the function of $\delta_{31,1}$ for other given parameters. However, the extreme values of η_2 and G_2 correspond to the poles

$$\delta_{32,2}^{(\pm)} = -\frac{1}{2}\left(\Delta_{21,1} - i\frac{\Gamma_{31}+\Gamma_{32}}{2}\right) \pm \frac{1}{2}\Delta_{21} \equiv \delta_{32}^{(\pm)}\left(\Delta_{21,1}\right) \tag{52}$$

of η_2, which is the function of $\delta_{31,2}$ for other given parameters. Here, the parameter $\Delta_{21,1}$ is given by

$$\Delta_{21} = \sqrt{\left(\Delta_{21,1} + i\frac{\Gamma_{32}-\Gamma_{31}}{2}\right)^2 + 4\Omega_{21,1}^2}. \tag{53}$$

To simplify following discussions, we assume that the points corresponding to the extreme values are well separated from each other, that is, $\sqrt{\Delta_{21,1}^2 + 4\Omega_{21,1}^2} \gg \Gamma_{31}/2, \Gamma_{32}/2$.

Let us study the maximum conversion efficiency and minimum attenuation for the conditions

$$\delta_{31,1} = \mathrm{Re}(\delta_{31,1}^{(\pm)}), \tag{54}$$

for η_1, G_1, and R_1, in the down conversion case, shown in the up panel of Fig. 1(b), and also

$$\delta_{32,2} = \mathrm{Re}(\delta_{32,2}^{(\pm)}), \tag{55}$$

for η_2, G_2 and R_2 in the up conversion case, shown in the down panel of Fig. 1(a). Under these conditions, the conversion efficiencies, attenuation rates and reflection coefficients are denoted by $\eta_{k\pm}^{\mathrm{I}}$, $G_{k\pm}^{\mathrm{I}}$, and $R_{k\pm}^{\mathrm{I}}$ with $k=1,2$.

Let us discuss the attenuation rate and the frequency conversion efficiency at the point, e.g., $f=0.51$, for the magnetic flux bias. Thus the decay rates can be determined as shown in Figs. 2(b)-(d). In Fig. 3, $|\eta_{k\pm}^{\mathrm{I}}|$ and $|G_{k\pm}^{\mathrm{I}}|$ are plotted as a function of $\Delta_{21,1}/2\pi$ for given driving strengths $\Omega_{21,1}/2\pi = 45\,\mathrm{MHz}$ or $\Omega_{21,1}/2\pi = 140\,\mathrm{MHz}$, respectively. And so are $\arg(R_{k\pm}^{\mathrm{I}})$ in Fig. 4. It is obvious that $|\eta_{k\pm}^{\mathrm{I}}|$, $|G_{k\pm}^{\mathrm{I}}|$, and $\arg(R_{k\pm}^{\mathrm{I}})$ are determined by the driving detuning $\Delta_{21,1}/2\pi$ for given driving strength $\Omega_{21,1}$ and all decay rates.

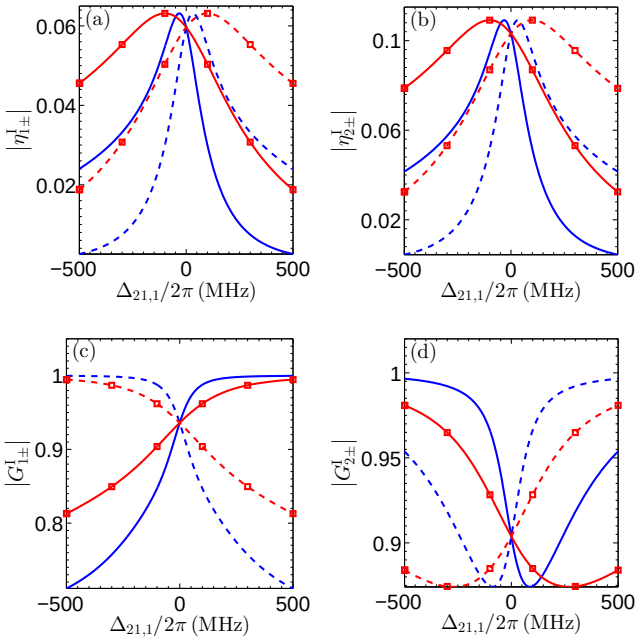

FIG. 3: (Color online) Driving type (1). Conversion efficiencies $|\eta_{1\pm}^{\mathrm{I}}|$ in (a) and $|\eta_{2\pm}^{\mathrm{I}}|$ in (b), and attenuation rates $|G_{1\pm}^{\mathrm{I}}|$ in (c) and $|G_{2\pm}^{\mathrm{I}}|$ in (d) are plotted as functions of the driving detuning $\Delta_{21,1}/2\pi$. In all subplots (a)-(d), the blue solid and dashed curves correspond to the driving strength $\Omega_{21,1}/2\pi = 45\,\mathrm{MHz}$, while the red ones marked with squares correspond to the driving strength $\Omega_{21,1}/2\pi = 140\,\mathrm{MHz}$. In (a) and (c), the dashed curves are for the probing detuning $\delta_{31,1} = \mathrm{Re}(\delta_{31,1}^{(-)})$ while the solid ones are for the probing detuning $\delta_{31,1} = \mathrm{Re}(\delta_{31,1}^{(+)})$. In (b) and (d), the dashed lines are for the probing detuning $\delta_{32,2} = \mathrm{Re}(\delta_{32,2}^{(-)})$ while the solid ones are for the probing detuning $\delta_{32,2} = \mathrm{Re}(\delta_{32,2}^{(+)})$. The values of other related parameters are taken from Fig. 2 and the reduced bias magnetic flux is taken as $f = 0.51$.

From Figs. 3(a)-(d), we find that the solid and dashed curves with the same color plotted according to Eqs. (54) and (55) are symmetric with the axis $\Delta_{21,1}/2\pi = 0$. We now take Fig. 3(a) as an example to justify this feature. From Eq. (51), we know that $\delta_{31,1}^{(\pm)}$ depends on $\Delta_{21,1}$. Assuming $\delta_{31,1} = \mathrm{Re}[\delta_{31}^{(+)}(\Delta_{21,1})]$ and $\delta'_{31,1} = \mathrm{Re}[\delta_{31}^{(-)}(-\Delta_{21,1})]$, we can easily find that $\delta'_{31,1} = -\delta_{31,1}$. We also get aware from Eq. (41) that η_1 is the function of $\delta_{31,1}$ and $\Delta_{21,1}$. Then using

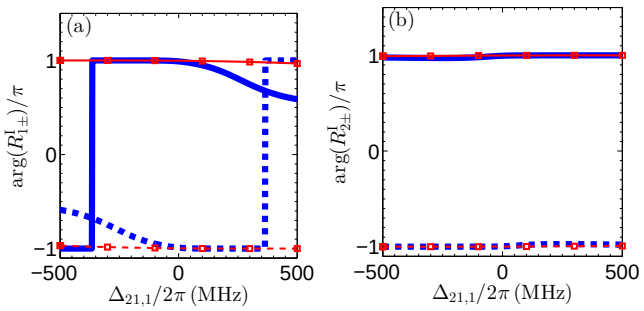

FIG. 4: (Color online) Driving type (1). Phases of the reflection coefficients (a) $\arg(R^{\rm I}_{1\pm})$ and (b) $\arg(R^{\rm I}_{2\pm})$, are plotted as functions of the driving detuning $\Delta_{21,1}/2\pi$. In both subplots (a) and (b), the blue solid and dashed curves are for the driving strength $\Omega_{21,1}/2\pi = 45\,\mathrm{MHz}$, while the red ones marked with squares are for the driving strength $\Omega_{21,1}/2\pi = 140\,\mathrm{MHz}$. In (a), the dashed lines are for the probing detuning $\delta_{31,1} = \mathrm{Re}(\delta^{(-)}_{31,1})$ while the solid ones are for the probing detuning $\delta_{31,1} = \mathrm{Re}(\delta^{(+)}_{31,1})$. In (b), the dashed curves are for the probing detuning $\delta_{32,2} = \mathrm{Re}(\delta^{(-)}_{32,2})$ while the solid ones are for the probing detuning $\delta_{32,2} = \mathrm{Re}(\delta^{(+)}_{32,2})$. The values of other related parameters are taken from Fig. 2 and the reduced bias magnetic flux is taken as $f = 0.51$.

Eqs. (41) and (51), the following relation can be verified, i.e.,

$$\left|\eta^{\rm I}_{1+}\left(\Delta_{21,1},\Omega_{21,1}\right)\right| = \left|\eta^{\rm I}_{1-}\left(-\Delta_{21,1},\Omega_{21,1}\right)\right|. \qquad (56)$$

Thus, the symmetric property of Fig. 3(a) is justified. The symmetric properties in Figs. 3(b)-(d) can also be justified, in a similar way as in Eq. (56).

The extreme values of $|G^{\rm I}_{k\pm}|$ and $|\eta^{\rm I}_{k\pm}|$ corresponding to $\Delta_{21,1}$ can be studied through Figs. 3(a)-(d). We find, from Figs. 3(a), (b) and (d), that the local maximum values of $|\eta^{\rm I}_{1\pm}|$ and $|\eta^{\rm I}_{2\pm}|$ are above 0.062 and 0.108, respectively, that is, the conversion efficiencies are about 6% and 11% respectively. The local minimum value of $|G^{\rm I}_{2\pm}|$ is about 0.875. Obviously, the local minimum (maximum) values are namely the minimum (maximum) values. We find that the extreme values of $|\eta^{\rm I}_{1\pm}|$, $|\eta^{\rm I}_{2\pm}|$ and $|G^{\rm I}_{2\pm}|$ are insensitive to the variation of the driving strength $\Omega_{21,1}$. However, the extreme points will get farther away from the origin when $\Omega_{21,1}$ is increased. In Fig. 3(c), we do not find an extreme value for $|G^{\rm I}_{1\pm}|$, the minimum value occurs at the boundaries of the driving detuning $\Delta_{21,1}$. When $\Omega_{21,1}/2\pi = 45\,\mathrm{MHz}$ and $140\,\mathrm{MHz}$, $|G^{\rm I}_{1\pm}|$ can be about 0.71 and 0.81 respectively. Besides, when $\Omega_{21,1}$ is increased, achieving the same attenuation of the incident signal field requires a larger driving detuning.

We analyze the limitations of $|\eta_{k\pm}|$ and $|G_{k\pm}|$ when $\Delta_{21,1}$ gets larger through examining Figs. 3(a)-(d). Figure 3 shows that when the detuning magnitude $|\Delta_{21,1}| = |\omega_{21} - \omega_{d1}|$ is increased, the conversion efficiencies $|\eta^{\rm I}_{k\pm}|$ approach zero, while the attenuation rate $|G^{\rm I}_{2\pm}|$ approach unity. It is because when the detuning $\Delta_{21,1}$ is large enough, the three-level system is decoupled from the driving field and thus there is no frequency conversion of the signal fields, which explains why $|\eta^{\rm I}_{k\pm}|$ approach zero. The large detuning of the driving field will also make the qubit stay in the ground state, and results in the decoupling between the qubit the signal field $\varepsilon_{32,2}$, which explains why $|G^{\rm I}_{2\pm}|$ approach unity. But there are different behaviors for $|G^{\rm I}_{1\pm}|$ in Fig 3(d) when $\Delta_{21,1}$ approaches negative infinity or positive infinity. We now explain the reason by taking $|G^{\rm I}_{1+}|$ as an example. When $\Delta_{21,1}$ approaches negative infinity, according to Eq. (54), the signal field will be resonant to the applied levels, thus undergoing large reflection. Therefore, $|G^{\rm I}_{1+}|$ will approach a non-unity value. However, when $\Delta_{21,1}$ approaches positive infinity, according to Eq. (54), the signal field will be largely detuned from the applied levels, thus undergoing no reflection at all. Therefore, $|G^{\rm I}_{1+}|$ will approach unity.

The behaviors of $|\eta^{\rm I}_{k\pm}|$ and $|G^{\rm I}_{k\pm}|$ for the resonant driving $\Delta_{21,1} = \omega_{21} - \omega_{d1} = 0$ are demonstrated in Figs. 3(a)-(d), we find that both $|\eta^{\rm I}_{k}|$ and $|G^{\rm I}_{k}|$ are insensitive to the variations of driving strength $\Omega_{21,1}$ in this case. From Figs. 3(a)-(d), we also find that proper driving detuning usually helps achieve better device performance, namely, larger conversion efficiencies and attenuation rates, than those in the resonant driving.

We now analyze the reflection coefficients R_1 and R_2 via $\arg(R^{\rm I}_{k\pm})$ in Figs. 4(a) and (b). We find that the solid and dashed curves are symmetric about the origin. Similarly to the derivation of Eq. (56), we have the equation

$$R^{\rm I}_{k-}(-\Delta_{21,1},\Omega_{21,1}) = R^{\rm I}_{k+}(\Delta_{21,1},\Omega_{21,1})^*. \qquad (57)$$

Thus, the phases of $R_{k\pm}$ satisfies

$$\arg(R^{\rm I}_{k-}(-\Delta_{21,1},\Omega_{21,1})) = -\arg(R^{\rm I}_{k+}(\Delta_{21,1},\Omega_{21,1})), \qquad (58)$$

which explains the symmetric feature in Figs. 4(a) and (b).

We also find that the phase angles of the reflection coefficients are nearly $\pm\pi$ for the strong driving. In Fig. 4(a), the blue solid curve, corresponding to $\arg(R^{\rm I}_{1+})$ when $\Omega_{21,1}/2\pi = 45\,\mathrm{MHz}$, shows a little deviation from $\pm\pi$ when $\Delta_{21,1}$ becomes bigger. However, when the driving strength is further increased, i.e., $\Omega_{21,1}/2\pi = 140\,\mathrm{MHz}$, the deviation is significantly decreased, as shown in the red solid squared curve. The similar phenomenon also occurs to the dashed curves. By combining Fig. 3(c) with Fig. 4(a), we find that the smaller $|G^{\rm I}_{1\pm}|$ always makes the phase of the reflection coefficient $R^{\rm I}_{1\pm}$ close to $\pm\pi$. Guaranteed by Eq. (54), we can achieve the maximum magnitude of the reflection coefficient when the phases of the reflection coefficient are $\pm\pi$. Thus, the maximum attenuation can be obtained. The phenomenon for $R^{\rm I}_{2\pm}$ as shown in Fig. 4(b) can also similarly explained as for that of $R^{\rm I}_{1\pm}$.

2. *Microwave frequency conversion and attenuation with variations of magnetic flux bias*

To study how the conversion efficiencies and the attenuation rates change with the reduced flux bias f, for each f and given $\Omega_{21,1}$, we change the driving detuning $\Delta_{21,1}/2\pi$ from -500 MHz to 500 MHz, and take the maximum values of $\eta^{\rm I}_{k\pm}$ and minimum values of $G^{\rm I}_{k\pm}$ (corresponding to the maximum values of $R^{\rm I}_{k\pm}$), which are now denoted by $\eta^{\rm II}_{k\pm}$,

$G^{\rm II}_{k\pm}$ (and $R^{\rm II}_{k\pm}$). Without loss of generality, we only discuss $\eta^{\rm II}_{k-}$, $G^{\rm II}_{k-}$, and $R^{\rm II}_{k-}$ in the below. The f-dependent $|\eta^{\rm II}_{k-}|$ and $|G^{\rm II}_{k-}|$ have been plotted in Fig. 5 for $\Omega_{21,1}/2\pi = 45$ MHz and $\Omega_{21,1}/2\pi = 140$ MHz. And also, the f-dependent $\arg(R^{\rm II}_{k-})$ is plotted in Fig. 6 for the same parameters as in Fig. 5.

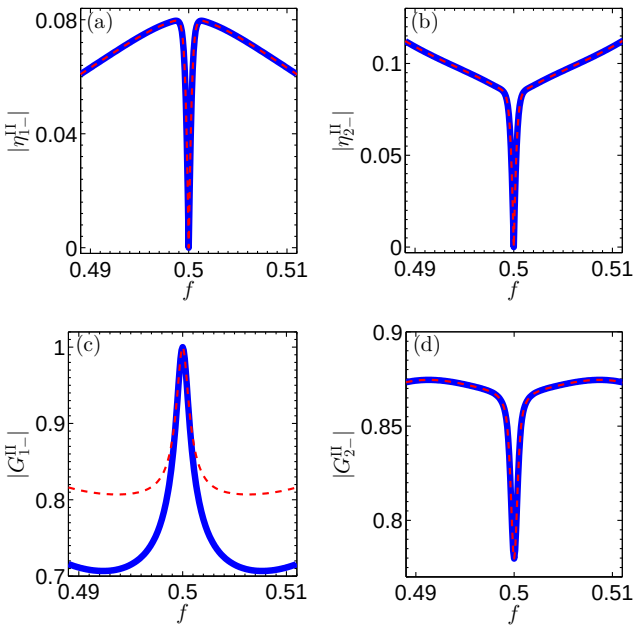

FIG. 5: (Color online) Driving type (1). Frequency conversion efficiencies $|\eta^{\rm II}_{1-}|$ in (a) and $|\eta^{\rm II}_{2-}|$ in (b), and attenuation rates $|G^{\rm II}_{1-}|$ in (c) and $|G^{\rm II}_{2-}|$ in (d) are plotted as functions of the reduced magnetic flux bias f. Here, the driving strength is taken as $\Omega_{21,1}/2\pi = 45$ MHz (blue solid curves) and $\Omega_{21,1}/2\pi = 140$ MHz (red dashed curves), respectively. When the reduced magnetic flux bias f is given, the driving detuning $\Delta_{21,1}$ changes in the range $-500\,{\rm MHz} \leq \Delta_{21,1}/2\pi \leq 500\,{\rm MHz}$, the values of the frequency conversion efficiencies $|\eta^{\rm II}_1|$ and $|\eta^{\rm II}_2|$, and attenuation rates $|G^{\rm II}_1|$ and $|G^{\rm II}_2|$ are taken as the maximum values of $|\eta^{\rm I}_1|$ and $|\eta^{\rm I}_2|$, and the minimum values of $|G^{\rm I}_1|$ and $|G^{\rm I}_2|$.

We now analyze the sensitivity of the conversion efficiencies $|\eta^{\rm II}_{k-}|$ and gains $|G^{\rm II}_{k-}|$ to the variation of the driving strength $\Omega_{21,1}$. For $|\eta^{\rm I}_{1-}|$, $|\eta^{\rm I}_{2-}|$, and $|G^{\rm I}_{2-}|$, the maximum value can be theoretically achieved in the range $-500\,{\rm MHz} \leq \Delta_{21,1}/2\pi \leq 500\,{\rm MHz}$ for given f, e.g., $f = 0.51$ as shown in Figs. 3(a), (b), and (d). Correspondingly, in Figs. 5(a), (b), and (d), we observe an obvious coincidence between the solid blue and dashed red curves, i.e., between the cases $\Omega_{21,1}/2\pi = 45$ MHz and $\Omega_{21,1}/2\pi = 140$ MHz. However, the maximum value of $|G^{\rm I}_{1-}|$ corresponds to infinite $\Delta_{21,1}/2\pi$ and cannot be theoretically achieved in the range $-500\,{\rm MHz} \leq \Delta_{21,1}/2\pi \leq 500\,{\rm MHz}$ for given f. We find an observable deviation between the solid blue and dashed red curves in Fig. 5(c).

As shown in Figs. 5(a)-(d), the optimally maximum values for the conversion efficiencies and optimally minimum values for the attenuation rates can be obtained in the ranges that $\Delta_{21,1}$ is taken from -500 MHz to 500 MHz and f is taken

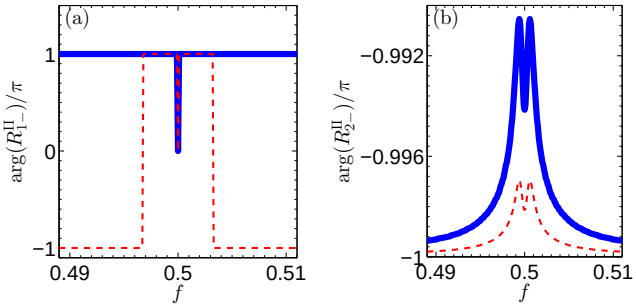

FIG. 6: (Color online) Driving type (1). Phases of the reflection coefficients $\arg(R^{\rm II}_1)$ in (a) and $\arg(R^{\rm II}_2)$ in (b) are plotted as functions of the reduced bias flux f. Here the driving frequency is taken as $\Omega_{21,1}/2\pi = 45\,{\rm MHz}$ (blue solid curves) $\Omega_{21,1}/2\pi = 140\,{\rm MHz}$ (red dashed curves). When the reduced bias flux f is permanent and the driving frequency $\Delta_{21,1}$ changes in the range $-500\,{\rm MHz} \leq \Delta_{21,1}/2\pi \leq 500\,{\rm MHz}$, the values of conversion efficiencies $|\eta^{\rm II}_1|$ and $|\eta^{\rm II}_2|$, and attenuation rates $|G^{\rm II}_1|$, and $|G^{\rm II}_2|$ are respectively taken the maximal values of conversion efficiencies $|\eta^{\rm I}_1|$ and $|\eta^{\rm I}_2|$, and the minimal values of attenuation rates $|G^{\rm I}_1|$ and $|G^{\rm I}_2|$.

from 0.49 to 0.51 for given $\Omega_{21,1}$, e.g., $\Omega_{21,1}/2\pi = 45$ MHz, and $\Omega_{21,1}/2\pi = 140$ MHz. In those parameter ranges, we find that the optimal conversion efficiency $|\eta^{\rm II}_{1-}|$ and $|\eta^{\rm II}_{2-}|$ are about 0.08 and 0.11, respectively. The optimal attenuation rate $|G^{\rm II}_{2-}|$ is about 0.775. The optimal attenuation rate $|G^{\rm II}_{1-}|$ is about 0.7 for $\Omega_{21,1}/2\pi = 45$ MHz and 0.8 for $\Omega_{21,1}/2\pi = 140$ MHz, respectively.

We know that the transition between $|1\rangle$ and $|3\rangle$ is prohibited when $f = 0.5$. Thus no reflection of the signal $\varepsilon_{31,1}$ is induced, i.e., $R^{\rm II}_{1-} = 0$, and we have $|G^{\rm II}_{1-}| = 1$ at $f = 0.5$, as shown in Fig. 5(c). The frequency conversion process can only be realized through the cyclic transition. That is, the prohibited transition between $|1\rangle$ and $|3\rangle$ induces $|\eta^{\rm II}_{1-}| = |\eta^{\rm II}_{2-}| = 0$ at $f = 0.5$, as shown in Figs. 5(a) and (b). Simultaneously, the prohibited transition makes the populations on the energy level $|3\rangle$ more easily decay to the energy level $|2\rangle$, thus resulting in significant reflection of the incident signal I_{p2}. That is why we see a sharp dip in Fig. 5(d).

From Figs. 6(a) and (b), we find that the phases of both $R^{\rm II}_{1-}$ and $R^{\rm II}_{2-}$ still keep quite close to $\pm\pi$ when the reduced flux bias f changes. It is not surprising because $|G^{\rm II}_{k-}|$ is the optimally maximum value of $|G^{\rm I}_{k-}|$ in a driving detuning range with each f and given $\Omega_{21,1}$, where $|G^{\rm I}_{k-}| < |G^{\rm I}_{k+}|$ must hold. As discussed for Figs. 3(e) and (f), the smaller one of $|G^{\rm I}_{k-}|$ and $|G^{\rm I}_{k+}|$ usually possesses a reflection coefficient which has a phase much closer to $\pm\pi$. At $f = 0.5$, $R^{\rm II}_{1-} = 0$, where the mathematically meaningless phase of $R^{\rm II}_{1-}$ is manually set $\arg(R^{\rm II}_{1-}) = 0$. This is the reason why we find a sharp dip at $f = 0.5$ in Fig. 6(a).

We find that the results in the driving type (2) are very similar to those of the driving type (1). In both types, the probing signals are not amplified. Thus for the compact of the main body of the paper, the detailed derivations and discussions of the driving type (2) have been given in Appendix B.

IV. MICROWAVE AMPLIFICATION, ATTENUATION, AND FREQUENCY CONVERSIONS IN THE DRIVING TYPE (3)

According to the analysis on the frequency conversion and the properties of the output signal field in both driving types (1) and (2). We find that the signal fields can only be attenuated and not be amplified in both cases. However the frequency conversion can be realized. We now study the frequency conversion and the amplification (or attenuation) of incident signal field for the driving type (3), in which the energy levels $|1\rangle$ and $|3\rangle$ are driven by the strong pump field, and the signal field is used to couple either the energy levels $|1\rangle$ and $|2\rangle$ or the energy levels $|2\rangle$ and $|3\rangle$. In this driving case, we find that the incident signal field can be amplified. The detailed analysis is given below.

A. Solutions

Using the same method as the derivations for the driving types (1) and (2), we can obtain the steady state solution of the reduced density matrix for the three-level system, which is considered as the zeroth order solution in the case of the driving type (3) when the signal filed is not applied. Those zeroth order solutions for the matrix elements are given as

$$s_{11}^{(0)}=\frac{\gamma_{21}}{X}\left[\Gamma_{31}\Omega_{31,3}^{2}+\frac{\Gamma_{31}^{2}}{4}(\gamma_{31}+\gamma_{32})+\Delta_{31,3}^{2}(\gamma_{31}+\gamma_{32})\right], \tag{59}$$

$$s_{22}^{(0)}=\frac{\Gamma_{31}\Omega_{31,3}^{2}\gamma_{32}}{X}, \tag{60}$$

$$s_{33}^{(0)}=\frac{\Gamma_{31}\Omega_{31,3}^{2}\gamma_{21}}{X}, \tag{61}$$

$$s_{13}^{(0)}=s_{31}^{(0)*}=\frac{i\Omega_{31,3}\gamma_{21}}{X}\left(\gamma_{31}+\gamma_{32}\right)\left(\frac{\Gamma_{31}}{2}+i\Delta_{31,3}\right), \tag{62}$$

with the parameter

$$X=\Gamma_{31}\Omega_{31,3}^{2}(2\gamma_{21}+\gamma_{32})+\gamma_{21}(\gamma_{31}+\gamma_{32})\left(\frac{\Gamma_{31}^{2}}{4}+\Delta_{31,3}^{2}\right). \tag{63}$$

Here $\Delta_{31,3}=\omega_{31}-\omega_{d3}$ is the detuning between the frequency of the driving field and the transition frequency between the energy levels $|1\rangle$ and $|3\rangle$. Hereafter, $\Delta_{31,3}$ is also called as the driving detuning. The other density matrix elements in the zeroth order approximation are zero, i.e., $s_{21}^{(0)}=s_{12}^{(0)}=s_{23}^{(0)}=s_{32}^{(0)}=0$. Without making confusion, here we still use $s_{mn}^{(r)}$ to denote the solution of the reduced density matrix elements of the three-level system in each order r for the driving type (3).

From the solution of the reduced density operator, we can find that the driving field induces the population change on energy levels $|1\rangle$,$|2\rangle$, and $|3\rangle$, and it polarizes the energy levels $|1\rangle$ and $|3\rangle$. Using the solution of the zeroth order approximation, we obtain nonzero solutions

$$\tilde{s}_{21}^{(1)}\left(\omega_{1}\right)=\frac{i\varepsilon_{21}}{Y}\left[Y_{1}s_{22-11}^{(0)}-i\Omega_{31,3}s_{13}^{(0)}\right], \tag{64}$$

$$\tilde{s}_{23}^{(1)}\left(\omega_{1}\right)=\frac{i\varepsilon_{21}}{Y}\left[i\Omega_{31,3}s_{22-11}^{(0)}-Y_{2}s_{13}^{(0)}\right], \tag{65}$$

of the matrix elements for the reduced density operator in the first order approximation. This solution corresponds to the case that the signal field is applied to the energy levels $|1\rangle$ and $|2\rangle$. Here, the parameters are defined as $s_{22-11}^{(0)}=s_{22}^{(0)}-s_{11}^{(0)}$, the detuning $\delta_{21,5}=\omega_{21}-\omega_{5}$, and $Y=Y_{1}Y_{2}+\Omega_{31,3}^{2}$ with

$$Y_{1}=i\delta_{21,5}-i\Delta_{31,3}+\frac{\Gamma_{32}}{2}, \tag{66}$$

$$Y_{2}=i\delta_{21,5}+\frac{\Gamma_{21}}{2}. \tag{67}$$

Then nonzero solutions corresponding to the signal field applied to the energy levels $|2\rangle$ and $|3\rangle$ can also be given as

$$\tilde{s}_{12}^{(1)}\left(-\omega_{6-}\right)=\frac{i\varepsilon_{32}}{Z}\left[Z_{2}s_{13}^{(0)}-i\Omega_{31,3}s_{33-22}^{(0)}\right], \tag{68}$$

$$\tilde{s}_{32}^{(1)}\left(-\omega_{6-}\right)=\frac{i\varepsilon_{32}}{Z}\left[Z_{1}s_{33-22}^{(0)}-i\Omega_{31,3}s_{13}^{(0)}\right]. \tag{69}$$

Here, the parameters are defined by $s_{33-22}^{(0)}=s_{33}^{(0)}-s_{22}^{(0)}$, the detuning $\delta_{32,6}=\omega_{32}-\omega_{6}$, and $Z=Z_{1}Z_{2}+\Omega_{31,3}^{2}$ with

$$Z_{1}=\left(i\delta_{32,6}-i\Delta_{31,3}+\frac{\Gamma_{21}}{2}\right), \tag{70}$$

$$Z_{2}=\left(i\delta_{32,6}+\frac{\Gamma_{32}}{2}\right). \tag{71}$$

Hereafter, both $\delta_{21,5}$ and $\delta_{32,6}$ are called as signal field detunings. Thus, in the coordinate of the experimental laboratory, we have

$$\tilde{s}_{E,21}^{(1)}\left(t\right)=\tilde{s}_{21}^{(1)}\left(\omega_{5}\right)e^{-i\omega_{5}t}+\tilde{s}_{21}^{(1)}\left(\omega_{6-}\right)e^{-i\omega_{6-}t}, \tag{72}$$

$$\tilde{s}_{E,32}^{(1)}\left(t\right)=\tilde{s}_{32}^{(1)}\left(-\omega_{5}\right)e^{-i\omega_{5+}t}+\tilde{s}_{32}^{(1)}\left(-\omega_{6-}\right)e^{-i\omega_{6}t}, \tag{73}$$

with the detunings $\omega_{5+}=\omega_{d3}-\omega_{5}$ and $\omega_{6-}=\omega_{d3}-\omega_{6}$.

B. Efficiencies of down and up conversions

In the driving type (3), we assume that the magnetic flux bias is near the optimal point [6]. Then we have $\omega_{32}>\omega_{21}$, as shown in Fig.1(a). It is clear that we can have a frequency up conversion process when the signal field is applied between the energy levels $|1\rangle$ and $|2\rangle$. In this case, the three-level system can emit one photon with the frequency ω_{5+} through the channel $|3\rangle\rightarrow|2\rangle$ induced by the signal field and the driving field. Similar to the driving type (1), the up conversion efficiency can be calculated as

$$\eta_{5}=\frac{\gamma_{32}I_{12}e^{-i\varphi_{5}}}{2I_{32}Y^{*}}\left[i\Omega_{31,3}s_{22-11}^{(0)}+Y_{2}^{*}s_{31}^{(0)}\right], \tag{74}$$

with

$$\varphi_5 = 2\arg\left[\tilde{I}_{p5}\left(0\right)\right]. \tag{75}$$

It is also found that a frequency down conversion process can occur when the signal field is applied between the energy levels $|2\rangle$ and $|3\rangle$. In this case, the down conversion efficiency can be given by

$$\eta_6 = \frac{\gamma_{21} I_{23} e^{-i\varphi_6}}{2 I_{21} Z^*}\left[-Z_2^* s_{31}^{(0)} - i\Omega_{31,3} s_{33-22}^{(0)}\right], \tag{76}$$

with

$$\varphi_6 = 2\arg\left[\tilde{I}_{p6}\left(0\right)\right]. \tag{77}$$

C. Gains of incident signal fields

In the driving types (1) and (2), the frequency conversion process takes away energy from the signal field, thus the signal field cannot be amplified. However, in the driving type (3), one part of the energy of the driving field can be transferred to the converted signal, other part can be transferred to the probing field, thus the signal field might be amplified. Because the signal can also be reflected, thus we expect that either amplification or attenuation of the signal field can occur. By taking the same procedure as for the driving types (1) and (2), the gain of the signal current corresponding to the frequency ω_5 can be given as

$$G_5 = 1 + R_5. \tag{78}$$

with the reflection coefficient

$$R_5 = -\frac{\gamma_{21}}{2Y}\left[-Y_1 s_{22-11}^{(0)} + i\Omega_{31,3} s_{13}^{(0)}\right] \tag{79}$$

However, the gain of the signal current corresponding to the frequency ω_6 is

$$G_6 = 1 + R_6, \tag{80}$$

with the reflection coefficient

$$R_6 = -\frac{\gamma_{32}}{2Z}\left[-Z_1 s_{33-22}^{(0)} + i\Omega_{31,3} s_{13}^{(0)}\right]. \tag{81}$$

Here, we use the gain to characterize the properties of the output field with the same frequency as the incident signal field although there might also be an attenuation. The signal is amplified when $|G_k| > 1$ (with $k = 5,\, 6$), otherwise, it is attenuated.

D. Discussions and numerical calculations

The nonlinear processes here are similar to those discussed in driving type (1), except that not only attenuation, but also amplification of the incident signal can occur. We now summarize the parameters that determine the gains G_k and the conversion efficiencies η_k with $k = 3,\, 4$. Similar to the driving type (1), the parameters G_k and η_k are determined by $\Delta_{31,3}$, $\Omega_{31,3}$ and the decay rates γ_{mn}, as well as $\delta_{21,5}$ for $k = 3$, or $\delta_{32,6}$ for $k = 4$. Also the decay rates γ_{mn} depend on f.

We now study how the extreme values can be obtained by varying the frequency of the signal field through the probing detuning $\delta_{21,5}$ or $\delta_{32,6}$. We know that the extreme values are related to the poles

$$\delta_{21,5}^{(\pm)} = \frac{1}{2}\left(\Delta_{31,3} - i\frac{\Gamma_{32}-\Gamma_{21}}{2}\right) \pm \frac{1}{2}\Delta_{31}, \tag{82}$$

of η_5 (corresponding to the gain G_5) from Eq. (74) and the poles

$$\delta_{32,6}^{(\pm)} = \frac{1}{2}\left(\Delta_{31,3} - i\frac{\Gamma_{21}+\Gamma_{32}}{2}\right) \pm \frac{1}{2}\Delta_{31}^*. \tag{83}$$

of η_6 (corresponding to the gain G_6) from Eq. (76). Here, the parameter Δ_{31} is defined as

$$\Delta_{31} = \sqrt{\left[\Delta_{31,3} - i\frac{\Gamma_{32}-\Gamma_{21}}{2}\right]^2 + 4\Omega_{31,3}^2}. \tag{84}$$

To simplify the discussion, we assume that the points corresponding to the extreme values are well separated from each other, that is, $\sqrt{\Delta_{31,3}^2 + 4\Omega_{31,3}^2} \gg \Gamma_{21}/2, \Gamma_{32}/2$.

1. *Microwave frequency conversion, amplification, and attenuation with variations of driving detuning*

We now study the maximum conversion efficiencies and maximum and minimum gains with the conditions

$$\delta_{21,5} = \mathrm{Re}\{\delta_{21,5}^{(\pm)}\}, \tag{85}$$

for η_5, G_5, and R_5, and

$$\delta_{32,6} = \mathrm{Re}\{\delta_{32,6}^{(\pm)}\}, \tag{86}$$

for η_6, G_6, and R_6. Under these conditions, the conversion efficiencies, gains and reflection coefficients are denoted by $\eta_{k\pm}^{\mathrm{I}}$, $G_{k\pm}^{\mathrm{I}}$, and $R_{k\pm}^{\mathrm{I}}$ with $k = 5,\, 6$. We take the magnetic flux bias as $f = 0.51$. In Fig. 7, $|\eta_{k\pm}^{\mathrm{I}}|$, and $|G_{k\pm}^{\mathrm{I}}|$ are plotted as functions of $\Delta_{31,3}/2\pi$ for driving strengths $\Omega_{31,3}/2\pi = 45\,\mathrm{MHz}$ and $\Omega_{31,3}/2\pi = 140\,\mathrm{MHz}$, respectively. And so are $\arg(R_{k\pm}^{\mathrm{I}})$ in Fig. 8. For a given driving strength $\Omega_{31,3}$, the magnitudes of conversion efficiencies $\eta_{k\pm}^{\mathrm{I}}$ and gains $G_{k\pm}^{\mathrm{I}}$ are determined by the driving detuning $\Delta_{31,3}/2\pi$.

From Figs. 7(a)-(d), we find that the solid and dashed curves with the same color, plotted according to Eqs. (85) and (86), are symmetric about the axis $\Delta_{31,3}/2\pi = 0$. The reasons for these features are similar to those in the driving type (1). We also find that corresponding to $\Delta_{31,3}$, the local maximum values of $|\eta_{5\pm}^{\mathrm{I}}|$ and $|\eta_{6\pm}^{\mathrm{I}}|$ are above 0.044 and 0.032, respectively. The local maximum values of $|G_{5\pm}^{\mathrm{I}}|$ and $|G_{6\pm}^{\mathrm{I}}|$

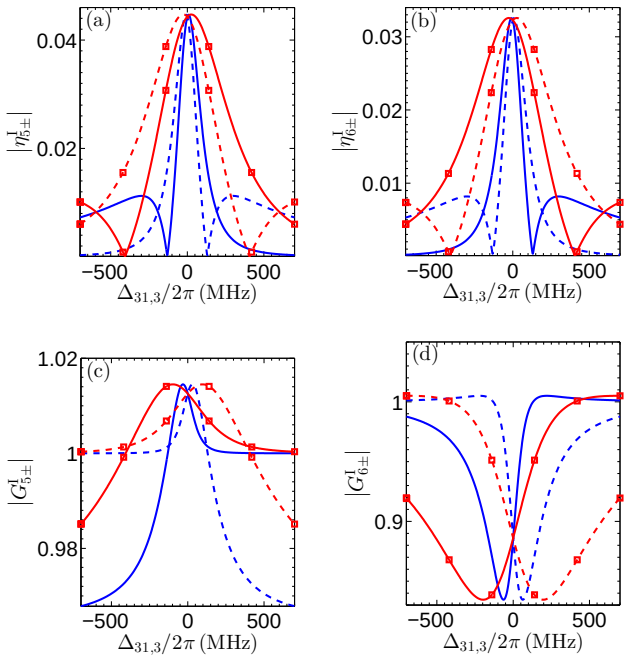

FIG. 7: (Color online) Driving type (3). Conversion efficiencies $|\eta^{\rm I}_5|$ in (a) and $|\eta^{\rm I}_6|$ in (b), and gains $|G^{\rm I}_5|$ in (c) and $|G^{\rm I}_6|$ in (d) are plotted as functions of the driving detuning $\Delta_{31,3}/2\pi$. In all subplots (a)-(d), the blue solid and dashed curves correspond to the driving strength $\Omega_{31,3}/2\pi = 45\,\mathrm{MHz}$, while the red ones marked with squares correspond to the driving strength $\Omega_{31,3}/2\pi = 140\,\mathrm{MHz}$. In (a) and (c), the dashed curves are for the probing detuning $\delta_{21,5} = \mathrm{Re}(\delta^{(-)}_{21,5})$ while the solid ones are for the probing detuning $\delta_{21,5} = \mathrm{Re}(\delta^{(+)}_{21,5})$. In (b) and (d), the dashed curves are for the probing detuning $\delta_{32,6} = \mathrm{Re}(\delta^{(-)}_{32,6})$, while the solid ones are for the probing detuning $\delta_{32,6} = \mathrm{Re}(\delta^{(+)}_{32,6})$. The values of other related parameters are taken from Fig. 2 and the reduced magnetic flux bias is taken as $f = 0.51$.

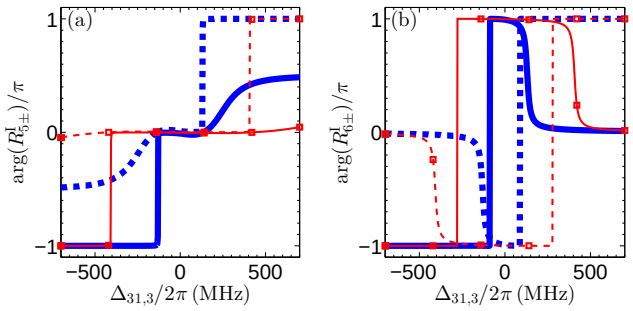

FIG. 8: (Color online) Driving type (3). Phases of the reflection coefficients (a) $\arg(R^{\rm I}_5)$ and (b) $\arg(R^{\rm I}_6)$, plotted as functions of the driving detuning $\Delta_{31,3}/2\pi$. In both subplots (a) and (b), the blue solid and dashed curves are for the driving strength $\Omega_{31,3}/2\pi = 45\,\mathrm{MHz}$, while the red ones marked with squares are for the driving strength $\Omega_{31,3}/2\pi = 140\,\mathrm{MHz}$. In (a), the dashed curves are for the probing detuning $\delta_{21,5} = \mathrm{Re}(\delta^{(-)}_{21,5})$ while the solid ones are for the probing detuning $\delta_{21,5} = \mathrm{Re}(\delta^{(+)}_{21,5})$. In (b), the dashed curves are for the probing detuning $\delta_{32,6} = \mathrm{Re}(\delta^{(-)}_{32,6})$, while the solid ones are for the probing detuning $\delta_{32,6} = \mathrm{Re}(\delta^{(+)}_{32,6})$. The values of other related parameters are taken from Fig. 2 and the reduced magnetic flux bias is taken as $f = 0.51$.

are about 1.014 and 1.008, respectively. This means the signal field is amplified. The local minimum value of $|G^{\rm I}_{6\pm}|$ is about 0.84. Obviously, the local minimum (maximum) values are namely the minimum (maximum) values. The local maximum values of $|\eta^{\rm I}_{5\pm}|$ and $|G^{\rm I}_{5\pm}|$, and local minimum values of $|G^{\rm I}_{6\pm}|$ are insensitive to the variation of the driving strength $\Omega_{31,3}$. These extreme value points will get farther away from the origin when $\Omega_{31,3}$ is increased. In Fig. 7(c), we do not find the local minimum value for $|G^{\rm I}_{5\pm}|$. Thus, the minimum $|G^{\rm I}_{5\pm}|$ occurs at the boundaries of the driving detuning $\Delta_{31,3}$. When $\Omega_{31,3}/2\pi = 45\,\mathrm{MHz}$ and $140\,\mathrm{MHz}$, the values about 0.968 and 0.986 can be achieved for $|G^{\rm I}_{5+}|$ and $|G^{\rm I}_{5-}|$, respectively. Besides, when $\Omega_{31,3}$ is increased, the same amount of the attenuation of the signal field will require larger driving detunings.

We now discuss the transition between attenuation and amplification. In Fig. 8(a), we find that there is a sharp transition from $-\pi$ to 0 for $\arg(R^{\rm I}_{5+})$, that is, the transition from attenuation to amplification. Due to continuity, $|G^{\rm I}_{5+}| = 1$ corresponds to the transparency, at the transition point. This indicates that the probing power is conserved and therefore no frequency conversion will occur. Thus, at the transition point, $|\eta^{\rm I}_{5+}| = 0$. The transition point will shift to the left when $\Omega_{31,3}$ is increased. Due to the symmetric property between the solid curves and the dashed ones, we do not discuss the latter. As shown in Figs. 7(b), (d), and Fig. 8(b) there are similar phenomena when the signal field is applied energy levels $|2\rangle$ and $|3\rangle$. But no obvious deviation from 0 and $\pm\pi$ exists in Fig. 8(b).

We now analyze the limitations of $|\eta_{k\pm}|$ and $|G_{k\pm}|$ when $\Delta_{31,3}$ gets larger through examining Figs. 7(a)-(d). Figure 7 shows when the detuning magnitude $|\Delta_{31,3}| = |\omega_{31} - \omega_{d3}|$ is increased, the conversion efficiencies $|\eta^{\rm I}_{k\pm}|$ will approach zero, while the gain $|G^{\rm I}_{6\pm}|$ will approach unity. It is because when the detuning $\Delta_{31,3}$ is large enough, the three-level system is decoupled from the driving field, and thus there is no frequency conversion of the probing fields, which explains why $|\eta^{\rm I}_{k\pm}|$ approach zero. The large driving detuning will also make the three-level system stay in the ground state, and results in the decoupling between the three-level system and the signal field, which explains why $|G^{\rm I}_{6\pm}|$ approaches unity. But there are different behaviors for $|G^{\rm I}_{5\pm}|$ in Fig 7(d) whether $\Delta_{31,3}$ approaches negative or positive infinity. We now explain the reason by taking $|G^{\rm I}_{5+}|$ as an example. When $\Delta_{31,3}$ approaches negative infinity, according to Eq. (85), the signal field is resonantly applied to the three level system, thus undergoing large reflection. Therefore, $|G^{\rm I}_{5+}|$ will approach a non-unity value. However, when $\Delta_{31,3}$ approaches positive infinity, according to Eq. (85), the signal field will be largely detuned from the three-level system, thus undergoing no reflection at all. Therefore, $|G^{\rm I}_{5+}|$ will approach unity.

From Figs. 7(a)-(d), we find that $|\eta^{\rm I}_k|$ and $|G^{\rm I}_k|$ are insensi-

tive to the variation of driving strength $\Omega_{31,3}$ when $\Delta_{31,3} = \omega_{31} - \omega_{d3} = 0$. In contrast to the resonant driving, better device performance, namely, larger conversion efficiencies, attenuations or amplifications, can be obtained by properly choosing the driving detuning.

In Figs. 8(a)-(b), the solid and dashed curves are symmetric about the origin. The reasons for these features are similar to those in the driving type (1). We also find that for the strong driving, the reflection coefficient phases are nearly $\pm\pi$ or 0. In Fig. 8(a), the blue solid curve, i.e., the curve for $\arg(R^{\rm I}_{5+})$ when $\Omega_{31,3}/2\pi = 45\,{\rm MHz}$, shows a little deviation from 0, when $\Delta_{31,3}$ gets larger. But when the driving strength is increased, i.e., $\Omega_{31,3}/2\pi = 140\,{\rm MHz}$, the deviation shows significant decrease, as shown by the red solid squared curve. The similar phenomenon also occurs to the dashed curves. By comparison of Fig. 7(c) and Fig. 8(a), we find that the smaller one of $|G^{\rm I}_{5+}|$ and $|G^{\rm I}_{5-}|$ always corresponds to a reflection coefficient whose phase is much closer to $\pm\pi$, and the bigger one of $|G^{\rm I}_{5+}|$ and $|G^{\rm I}_{5-}|$ always corresponds to a reflection coefficient whose phase is much closer to 0. Guaranteed by Eq. (85), we can achieve the maximum magnitude of the reflection coefficient. The phases $\pm\pi$ or 0 will further make sure that the optimal attenuation or amplification is achieved.

2. *Microwave frequency conversion, amplification, and attenuation with variations of magnetic flux bias*

We now study how the conversion efficiencies and the gain change with the reduced magnetic flux bias f. For given $\Omega_{31,3}$ and each f, we change the driving detuning $\Delta_{31,3}/2\pi$ from -700 MHz to 700 MHz, and take the optimal $\eta^{\rm I}_{k\pm}$, $G^{\rm I}_{k\pm}$, and $R^{\rm I}_{k\pm}$, which are now denoted by $\eta^{\rm II}_{k\pm}$, $G^{\rm II}_{k\pm}$, $R^{\rm II}_{k\pm}$, $\bar{G}^{\rm II}_{k\pm}$, and $\bar{R}^{\rm II}_{k\pm}$ with $k = 5, 6$. Here, $G^{\rm II}_{k\pm}$ and $R^{\rm II}_{k\pm}$ correspond to the minimum values while $\bar{G}^{\rm II}_{k\pm}$ and $\bar{R}^{\rm II}_{k\pm}$ correspond to maximum values. Without loss of generality, below we only discuss $\eta^{\rm II}_{k-}$, $G^{\rm II}_{k-}$, and $R^{\rm II}_{k-}$. The f-dependent $|\eta^{\rm II}_{k-}|$, $|G^{\rm II}_{k-}|$, $\arg(R^{\rm II}_{k-})$, and $|\bar{G}^{\rm II}_{k-}|$ are plotted in Fig. 9, for $\Omega_{31,3}/2\pi = 45$ MHz and $\Omega_{31,3}/2\pi = 140\,{\rm MHz}$, respectively. And so are $\arg(\bar{R}^{\rm II}_{k-})$ in Fig. 10.

We now analyze the sensitivity of the conversion efficiencies $|\eta^{\rm II}_{k-}|$ and gains $|G^{\rm II}_{k-}|$, $|\bar{G}^{\rm II}_{k-}|$ to the variation of the driving strength $\Omega_{31,3}$. For $|\eta^{\rm I}_{k-}|$, $|G^{\rm I}_{2-}|$, and $|\bar{G}^{\rm I}_{k-}|$, the optimally minimum and maximum values can be achieved in the range $-700\,{\rm MHz} \le \Delta_{31,3}/2\pi \le 700\,{\rm MHz}$, as shown in Figs. 9(a), (b), and (d). Correspondingly, in Figs. 9(a), (b), (d), (e), and (f), we observe an obvious coincidence between the solid blue and dashed red curves, i.e., between the cases $\Omega_{31,3}/2\pi = 45$ MHz and $\Omega_{31,3}/2\pi = 140\,{\rm MHz}$. For $|G^{\rm I}_{5-}|$, the optimally minimum value, which means $\Delta_{31,3}/2\pi$ approaches infinity, cannot be achieved in the range $-700\,{\rm MHz} \le \Delta_{31,3}/2\pi \le 700\,{\rm MHz}$. We see an observable deviation between the solid blue and dashed red curves in Fig. 9(c).

From Figs. 9(a)-(d), we can find that the optimally maximum conversion efficiency $|\eta^{\rm II}_{5-}|$ and $|\eta^{\rm II}_{6-}|$ are respectively about 1.16 and 0.046. The optimally minimum value of $|G^{\rm II}_{5-}|$ is about 0.04 for $\Omega_{31,3}/2\pi = 45\,{\rm MHz}$ and 0.16 for $\Omega_{31,3}/2\pi = 140\,{\rm MHz}$. The optimally minimum value of $|G^{\rm II}_{6-}|$ is about 0.832. The signal fields are attenuated. The optimally maximum gains $|\bar{G}^{\rm II}_{5-}|$ and $|\bar{G}^{\rm II}_{6-}|$ are respectively about 1.048 and 1.104. That is, the signal fields are amplified.

If f gets infinitesimally close to 0.5, we find through Fig. 9(c) that $|G^{\rm II}_{5}|$ sharply approaches zero, which means the incident signal current $\tilde{I}_{p5}\,(0)$ is almost totally reflected. But the frequency conversion still works. This is because when f approaches 0.5, the ratio ω_{32}/ω_{21} becomes larger and larger as shown in Fig. 2(a), and thus the energy with $\omega_1 \approx \omega_{21}$ coming from the conversion process become less and less. So the nearly total reflection of the incident signal current $\tilde{I}_{p5}\,(0)$ is justified. Besides, the large value of $|\eta^{\rm II}_{5-}|$ is also induced at $f = 0.5$. However, $|\eta^{\rm II}_{6-}|$ is quite small and $|G^{\rm II}_{6-}|$ is nearly transparent near $f = 0.5$. This is also due to the large ratio of ω_{32}/ω_{21}.

From Figs. 9(e), (f), (i), and (j), we find that the phases of $R^{\rm II}_{k-}$ keep quite close to $\pm\pi$ and the ones of $\bar{R}^{\rm II}_{k-}$ keep quite close to 0. This is not surprising since $|G^{\rm II}_{k-}|$ is the minimum value of $|G^{\rm I}_{k-}|$ in the range of the driving detuning $\Delta_{31,3}$, where $|G^{\rm I}_{k-}| < |G^{\rm I}_{k+}|$ must hold. As the previous discussions on Figs. 7(e) and (f), the smaller one of $|G^{\rm I}_{k-}|$ and $|G^{\rm I}_{k+}|$ usually possesses a reflection coefficient which has a phase much closer to $\pm\pi$.

V. CONCLUSIONS AND DISCUSSIONS

In summary, using a three-level three-junction flux qubit circuit as an example, we study how the frequency conversion and signal amplification (or attenuation) can be realized when the inversion symmetry of the potential energy is broken. We mention that the microwave amplification has recently been experimentally realized [56, 57] in a three-level system constructed by four-junction flux qubit circuits. However, our study provides a full picture for understanding the microwave frequency conversion and amplification (or attenuation) in the case of all possible driving and probing.

Based on different configurations of the applied driving and probing fields, we classify our study into three types. We find that a single three-level superconducting flux qubit circuit is enough to complete the microwave frequency conversion, amplification (or attenuation) of weak signal fields. In particular, we find, (i) in the driving types (1) and (2), the three-level system can convert the driving and signal fields into the ones with new frequencies, which we call down conversion or up conversion, respectively. Due to the energy loss in the reflection and conversion, the incident signal field suffers the attenuation after transmitted in these two driving types; (ii) however, both amplification and attenuation can occur in the driving type (3), whether the amplification or the attenuation depends on the parameter condition; (iii) given a definite flux bias, when the driving and signal detunings are adjusted properly, the maximum conversion efficiencies and gains nearly do not depend on the driving strength.

Although our study focuses on a three-level superconducitng flux qubit circuit, the method used here can be easily

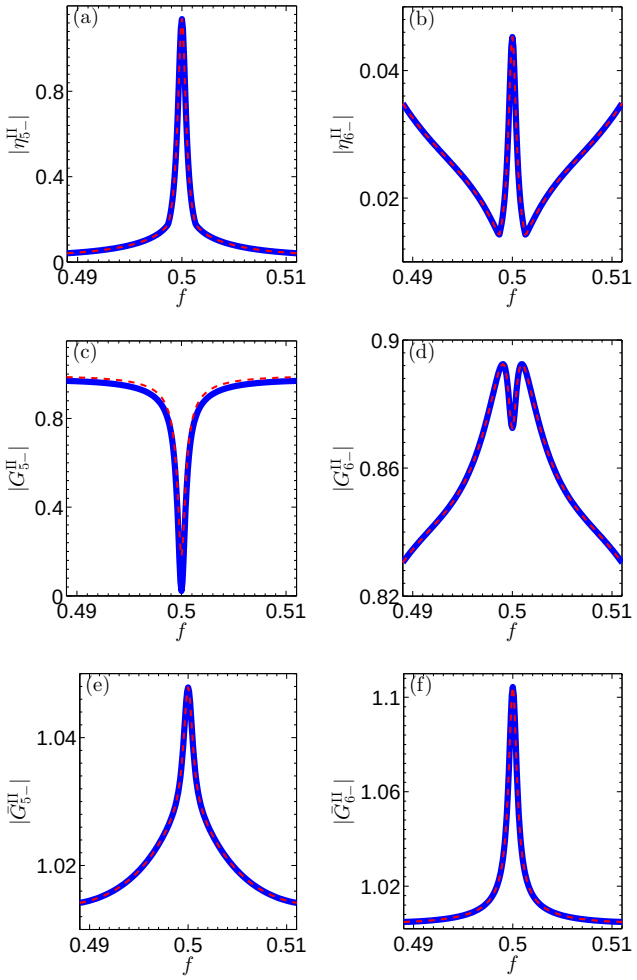

FIG. 9: (Color online) Driving type (3). Conversion coefficients $|\eta_5^{\rm II}|$ in (a) and $|\eta_6^{\rm II}|$ in (b), gains $|G_5^{\rm II}|$ in (c), $|G_6^{\rm II}|$ in (d), $|\bar{G}_5^{\rm II}|$ in (e), and $|\bar{G}_6^{\rm II}|$ in (f), are plotted as functions of the reduced flux bias f. Here the driving frequency is taken as $\Omega_{31,3}/2\pi = 45\,\mathrm{MHz}$ (blue solid curves) and $\Omega_{31,3}/2\pi = 140\,\mathrm{MHz}$ (red dashed curves). When the reduced flux bias f is given and the driving frequency $\Delta_{31,3}$ varies in the range $-700\,\mathrm{MHz} \leq \Delta_{31,3}/2\pi \leq 700\,\mathrm{MHz}$, the values of conversion efficiencies $|\eta_5^{\rm II}|$ and $|\eta_6^{\rm II}|$, and gains $|G_5^{\rm II}|$, $|G_6^{\rm II}|$, $|\bar{G}_5^{\rm II}|$, and $|\bar{G}_6^{\rm II}|$ respectively take the maximum values of conversion efficiencies $|\eta_5^{\rm I}|$ and $|\eta_6^{\rm I}|$, the minimum values of $|G_5^{\rm I}|$ and $|G_6^{\rm I}|$ and the maximum values of $|G_5^{\rm I}|$ and $|G_6^{\rm I}|$.

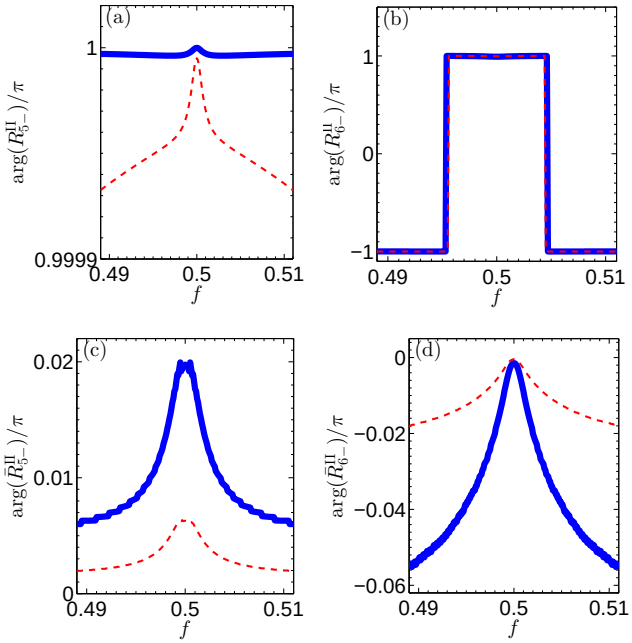

FIG. 10: (Color online) Driving type (3). Phases of the reflection coefficients $\arg(R_{5-}^{\rm II})$ in (a), $\arg(R_{6-}^{\rm II})$ in (b), $\arg(\bar{R}_{5-}^{\rm II})$ in (c), and $\arg(\bar{R}_{6-}^{\rm II})$ in (d) are plotted as functions of the reduced flux bias f. Here the driving frequency is taken as $\Omega_{31,3}/2\pi = 45\,\mathrm{MHz}$ (blue solid curves) and $\Omega_{31,3}/2\pi = 140\,\mathrm{MHz}$ (red dashed curves). When the reduced flux bias f is given and the driving frequency δ_{31} varies in the range $-700\,\mathrm{MHz} \leq \Delta_{31,3}/2\pi \leq 700\,\mathrm{MHz}$, the values of conversion efficiencies $|\eta_5^{\rm II}|$ and $|\eta_6^{\rm II}|$, and gains $|G_5^{\rm II}|$, $|G_6^{\rm II}|$, $|\bar{G}_5^{\rm II}|$, and $|\bar{G}_6^{\rm II}|$ respectively take the maximum values of conversion efficiencies $|\eta_5^{\rm I}|$ and $|\eta_6^{\rm I}|$, the minimum values of $|G_5^{\rm I}|$ and $|G_6^{\rm I}|$ and the maximum values of $|G_5^{\rm I}|$ and $|G_6^{\rm I}|$.

applied to a superconducting phase [45–47] and Xmon [48] qubit circuits or other quantum circuits in which the inversion symmetry of their potential energy is broken. In contrast to large anharmonicity of the flux qubit circuits, the superconducting phase and Xmon qubit circuits have small anharmonicity. Therefore the information leakage should be more carefully studied when these processes are demonstrated. We note that the transmon qubit circuits [59, 60] have well defined symmetry when the effective offset charge is at the optimal point, thus the transmon qubit circuit for its three lowest energy levels has ladder-type transitions, and the three-wave mixing cannot be realized. However, when the effective offset charge is not at the optimal point, the three-wave mixing can also occur in such system.

It is well known that single superconducting artificial atom can be strongly coupled to different quantized microwave fields through the circuit QED technique. For example, correlated emission lasing has been demonstrated using a single three-level flux qubit circuit which is coupled to two quantized microwave modes in a transmission line resonator, and a classical field is coherently converted into other two different mode fields of microwave fields. Thus, the semiclassical treatment here for microwave field can be easily modified to the quantum case. In this case, our model can be used to study controllable generation of single and entangled microwave photon states using a single artificial atom. This will be very important for quantum information processing on superconducting quantum chip.

Acknowledgments

YXL is supported by the National Basic Research Program of China Grant No. 2014CB921401, the NSFC Grants No.

61025022, and No. 91321208.

Appendix A: Decay rate derivation

The three-level flux qubit circuit here is coupled to a one-dimensional open transmission line though a mutual inductance M such that the model we study here can be modeled by the Hamiltonian shown in Eq. (1). To simplify the description, the system Hamiltonian is given by

$$H_S^{(l)} = \hbar\omega_{21}\sigma_{22} + \hbar\omega_{31}\sigma_{33} + H_R^{(l)}(t) + H_\varepsilon^{(l)}(t), \quad \text{(A1)}$$

and the Hamiltonian including the interaction between the system and the environment is given by

$$H^{(l)} = H_S^{(l)} + H_T^{(l)}, \quad \text{(A2)}$$

where

$$H_T^{(l)} = -M\hat{I}I_T(0,t). \quad \text{(A3)}$$

Here, $I_T(x,t)$ includes the quantum thermal noise currents that travel towards both left and right directions, each denoted by $I_L(x,t)$ and $I_R(x,t)$. Resorting to the canonical quantization treatment [50], we have

$$I_L(x,t) = \int_{-\infty}^{\infty} \mathrm{d}\omega\, \mathrm{sgn}(\omega)\, i\sqrt{\frac{\hbar|\omega|}{4\pi Z_T}} A_L(\omega)\, e^{-i\omega(t+x/v)}, \quad \text{(A4)}$$

$$I_R(x,t) = -\int_{-\infty}^{\infty} \mathrm{d}\omega\, \mathrm{sgn}(\omega)\, i\sqrt{\frac{\hbar|\omega|}{4\pi Z_T}} A_R(\omega)\, e^{-i\omega(t-x/v)}, \quad \text{(A5)}$$

with

$$[A_\alpha(\omega_1), A_\beta(\omega_2)] = \delta_{\alpha\beta}\delta(\omega_1+\omega_2)\,\mathrm{sgn}(\omega_1), \quad \text{(A6)}$$

$$A_\alpha^\dagger(\omega_1) = A_\alpha(-\omega_1), \quad \text{(A7)}$$

where $\mathrm{sgn}(\omega) = -1$, 0, or 1 for $\omega < 0$, $\omega = 0$, $\omega > 0$, respectively. Substituting Eqs. (A4 and A5) into Eq. (A3), we have

$$H_T^{(l)} = i\hbar\sum_{mn} b_{mn}^L(t)\,\sigma_{mn} + i\hbar\sum_{mn} b_{mn}^R(t)\,\sigma_{mn}, \quad \text{(A8)}$$

with

$$b_{mn}^L(t) = \frac{-MI_{mn}}{\hbar}\int_{-\infty}^{\infty} \mathrm{d}\omega\,\mathrm{sgn}(\omega)\sqrt{\frac{\hbar|\omega|}{4\pi Z_T}} A_L(\omega)\, e^{-i\omega t}, \quad \text{(A9)}$$

$$b_{mn}^R(t) = \frac{MI_{mn}}{\hbar}\int_{-\infty}^{\infty} \mathrm{d}\omega\,\mathrm{sgn}(\omega)\sqrt{\frac{\hbar|\omega|}{4\pi Z_T}} A_R(\omega)\, e^{-i\omega t}, \quad \text{(A10)}$$

we can easily find

$$[b_{mn}^\alpha(t)]^\dagger = -b_{mn}^\alpha(t). \quad \text{(A11)}$$

Adopting the idea in Refs. [51, 54], and using the fact

$$\langle A_\alpha(\omega)\, A_\alpha(\omega')\rangle = \mathrm{sgn}(\omega)\left(\bar{N}(\omega)+1\right)\delta(\omega+\omega'), \quad \text{(A12)}$$

with

$$\bar{N}(\omega) = \frac{1}{e^{\hbar\omega/k_BT}-1}, \quad \text{(A13)}$$

we have for $m \neq n$

$$\langle b_{mn}^\alpha(t)\, b_{nm}^\alpha(t')\rangle = \frac{|MI_{mn}|^2\hbar\omega_{mn}}{-2\hbar^2 Z_T}\left(\bar{N}(\omega_{mn})+1\right)\delta(t-t'). \quad \text{(A14)}$$

We consider here a common case that the environment temperature is not high enough to excite the three-level system, i.e., $|\hbar\omega_{ij}|/k_BT \gg 1$, which means for $m > n$,

$$\langle b_{mn}^\alpha(t)\, b_{nm}^\alpha(t')\rangle = -\frac{|MI_{mn}|^2\hbar\omega_{nm}}{2\hbar^2 Z_T}\delta(t-t'), \quad \text{(A15)}$$

while for $m < n$,

$$\langle b_{mn}^\alpha(t)\, b_{nm}^\alpha(t')\rangle = 0. \quad \text{(A16)}$$

Similarly,

$$\begin{aligned}\langle b_{mm}^\alpha(t)\, b_{nn}^\alpha(t')\rangle =& \frac{M^2 I_{mm}I_{nn}}{-2\hbar^2 Z_T}\lim_{\omega\to 0}\left(\bar{N}(\omega)+1\right)\hbar\omega\delta(t-t') \\ =& -\frac{M^2 I_{mm}I_{nn}k_BT}{2\hbar^2 Z_T}\delta(t-t'), \quad \text{(A17)}\end{aligned}$$

We define new parameters as follows,

$$\gamma_{mn} = \frac{|MI_{mn}|^2\hbar\omega_{mn}}{\hbar^2 Z_T}, m > n, \quad \text{(A18)}$$

$$\xi_{mn} = \frac{M^2 I_{mm}I_{nn}k_BT}{\hbar^2 Z_T}. \quad \text{(A19)}$$

Thus, using the Ito's rule, we have

$$\mathrm{d}B_{mn}^\alpha(t)\,\mathrm{d}B_{nm}^\alpha(t') = \frac{-\gamma_{mn}}{2}, m > n, \quad \text{(A20)}$$

$$\mathrm{d}B_{mm}^\alpha(t)\,\mathrm{d}B_{nn}^\alpha(t') = \frac{-\xi_{mn}}{2}. \quad \text{(A21)}$$

All the other products of second or higher orders vanish. Thus

$$\frac{H^{(l)}\mathrm{d}t}{i\hbar} = \frac{H_S^{(l)}\mathrm{d}t}{i\hbar} + \sum_{mn}\mathrm{d}B_{mn}^L(t)\,\sigma_{mn} + \sum_{mn}\mathrm{d}B_{mn}^R(t)\,\sigma_{mn}. \quad \text{(A22)}$$

Next we calculate the Ito generator $\mathrm{d}G$ following the method in Refs. [54, 55], i.e.,

$$\begin{aligned}\mathrm{d}G =& \exp\left(\frac{H^{(l)}\mathrm{d}t}{i\hbar}\right) - 1 \\ =& \frac{H_S\mathrm{d}t}{i\hbar} - \frac{1}{2}\sum_{m>n}\gamma_{mn}\sigma_{mm}\mathrm{d}t - \frac{1}{2}\sum_m \xi_{mm}\sigma_{mm}\mathrm{d}t \\ &+ \sum_{mn}\mathrm{d}B_{mn}^L(t)\,\sigma_{mn} + \sum_{mn}\mathrm{d}B_{mn}^R(t)\,\sigma_{mn}. \quad \text{(A23)}\end{aligned}$$

Then, we can obtain the master equation using $\mathrm{d}G$, i.e.,

$$\begin{aligned}\mathrm{d}P_E =& \mathrm{Tr}\left\{\mathrm{d}\hat{P}_E\right\} \\ =& \mathrm{Tr}\left\{\hat{P}_E \mathrm{d}G^\dagger\right\} + \mathrm{Tr}\left\{\mathrm{d}G\hat{P}_E\right\} + \mathrm{Tr}\left\{\mathrm{d}G\hat{P}_E\mathrm{d}G^\dagger\right\}.\end{aligned} \tag{A24}$$

Here, $\hat{P}_E$ is the composite density operator in the coordinate system of the experimental laboratory. Correspondingly, P_E is the reduced density operator with $\mathrm{Tr}\{\cdot\}$ meaning tracing out the environmental part. Taking the derivative of P_E with respect to the time t yields

$$\begin{aligned}\dot{P}_E =& \frac{\mathrm{d}P_E}{\mathrm{d}t} = \frac{1}{i\hbar}\left[H_S^{(l)}, P_E\right] \\ &+ \sum_{mn}\xi_{mn}\sigma_{mm}P_E\sigma_{nn} - \frac{1}{2}\sum_m \xi_{mm}\left(\sigma_{mm}P_E + P_E\sigma_{mm}\right) \\ &+ \frac{1}{2}\sum_{m>n}\gamma_{mn}\left(2\sigma_{nm}P_E\sigma_{mn} - \sigma_{mm}P_E - P_E\sigma_{nn}\right).\end{aligned} \tag{A25}$$

Equation (A25) can be further reduced to

$$\begin{aligned}\dot{P}_E =& \frac{\left[H_S^{(l)}, P_E\right]}{i\hbar} - \frac{1}{2}\sum_{m\neq n}\gamma_{mn}^{\phi}P_{E,mn}\sigma_{mn} \\ &+ \sum_{m>n}\frac{\gamma_{mn}}{2}\left(2\sigma_{nm}P_E\sigma_{mn} - \sigma_{mm}P_E - P_E\sigma_{mm}\right),\end{aligned} \tag{A26}$$

or in another form,

$$\begin{aligned}\dot{P}_E =& \frac{1}{i\hbar}\left[H_S^{(l)}, P_E\right] - \sum_{m\neq n}\frac{1}{2}\Gamma_{mn}P_{E,mn}\sigma_{mn}, \\ &+ \sum_m\left(\sum_{k>m}\gamma_{km}P_{E,kk} - \sum_{k<m}\gamma_{mk}P_{E,mm}\right)\sigma_{mm}\end{aligned} \tag{A27}$$

where $P_{E,mn}$ is the matrix element of P_E and

$$\gamma_{mn}^{\phi} = \frac{M^2 k_B T}{\hbar^2 Z_T}\left(I_{mm} - I_{nn}\right)^2, m > n, \tag{A28}$$

$$\Gamma_{mn} = \Gamma_{nm} = \sum_{k<m}\gamma_{mk} + \sum_{k<n}\gamma_{nk} + \gamma_{mn}^{\phi}, m > n. \tag{A29}$$

Now we have obtained the decay rates $\gamma_{mn}, \gamma_{mn}^{\phi}$ and Γ_{mn}, which are respectively called relaxation, pure dephasing, and total dephasing rates.

Appendix B: Attenuation and amplification in the driving type (2)

1. Solutions

Since the derivation in driving type (2) is similar to that in driving type (1), we will directly give the results in this section.

The zeroth order steady state is

$$\chi^{(0)} = \sigma_{11}, \tag{B1}$$

which means that the three-level system stays in the ground state.

The first order steady state then can be obtained through the iteration method using the zeroth steady state. First we expand the matrix elements of the density operator in its frequency domain just like Eq. (27). The nonzero results corresponding to the signal field applied to the energy levels $|1\rangle$ and $|3\rangle$ can be given as follows,

$$\tilde{\chi}_{21}^{(1)}\left(\nu_{21}\right) = \frac{\left(-i\Omega_{32,2}\right)\chi_{11}^{(0)}}{U_1U_2 + \Omega_{32,2}^2}\left(-i\varepsilon_{31,3}\right), \tag{B2}$$

$$\tilde{\chi}_{31}^{(1)}\left(\nu_{21}\right) = \frac{V_1\chi_{11}^{(0)}}{U_1U_2 + \Omega_{32,2}^2}\left(-i\varepsilon_{31,3}\right). \tag{B3}$$

Here, $\nu_{21} = \delta_{32,4} - \delta_{31,3}$, with the detunings $\Delta_{32,2} = \omega_{32} - \omega_{d2}$, and $\delta_{31,3} = \omega_{31} - \omega_3$. The parameters U_1 and U_2 are

$$U_1 = -i\Delta_{32,2} + i\delta_{31,3} + \frac{\Gamma_{21}}{2}, \tag{B4}$$

$$U_2 = i\delta_{31,3} + \frac{\Gamma_{31}}{2}. \tag{B5}$$

The nonzero results corresponding to the signal field applied to the energy levels $|1\rangle$ and $|2\rangle$ can also be given as follows,

$$\tilde{\chi}_{21}^{(1)}\left(-\delta_{21,4}\right) = \frac{U_1\chi_{11}^{(0)}}{V_1V_2 + \Omega_2^2}\left(-i\varepsilon_{21,4}\right), \tag{B6}$$

$$\tilde{\chi}_{31}^{(1)}\left(-\delta_{21,4}\right) = \frac{-i\Omega_2\chi_{11}^{(0)}}{V_1V_2 + \Omega_2^2}\left(-i\varepsilon_{21,4}\right). \tag{B7}$$

Here, the detuning $\delta_{21,4} = \omega_{21} - \omega_4$. The parameters V_1 and V_2 are

$$V_1 = i\delta_{21,4} + i\Delta_{32,2} + \frac{\Gamma_{31}}{2}, \tag{B8}$$

$$V_2 = i\delta_{21,4} + \frac{\Gamma_{21}}{2}. \tag{B9}$$

Hereafter, both δ_{31} and δ_{21} are called as signal field detunings. Thus in the coordinate of the experimental laboratory, we have

$$\tilde{\rho}_{E,21}^{(1)}(t) = \tilde{\chi}_{21}^{(1)}\left(-\delta_{21,4}\right)e^{-i\omega_4 t} + \tilde{\chi}_{21}^{(1)}\left(\nu_{21}\right)e^{-i\omega_{3-}t}, \tag{B10}$$

$$\tilde{\rho}_{E,31}^{(1)}(t) = \tilde{\chi}_{31}^{(1)}\left(-\delta_{21,4}\right)e^{-i\omega_{4+}t} + \tilde{\chi}_{31}^{(1)}\left(\nu_{21}\right)e^{-i\omega_3 t}, \tag{B11}$$

with the frequencies $\omega_{3-} = \omega_3 - \omega_{d2}$, and $\omega_{4+} = \omega_4 + \omega_{d2}$.

2. Efficiencies of down and up conversions

As shown in the top panel of Fig. 1(c) The physical process of frequency down conversion in driving type (2) is just

similar to that in driving type (1). First, the three-level system absorbs a photon of the probe field with the frequency ω_3 and is excited to the level $|3\rangle$. Then the three-level system emits a photon of the frequency ω_{d2} through the decay channel $|3\rangle \to |2\rangle$ and a photon of the new frequency ω_{3-} when operating as the energy conservation law demands. The down conversion efficiency can then be similarly expressed as,

$$\eta_3 = \frac{-\gamma_{21} I_{31}}{2 I_{21}} \frac{(-i\Omega_{32,2})\,\chi_{11}^{(0)}}{U_1 U_2 + \Omega_{32,2}^2}. \tag{B12}$$

The frequency up conversion in driving type (2) is also similar to that in driving type (1). First, the three-level system absorbs a photon of the probe field with the frequency ω_4 and a photon of the driving field with the frequency ω_{d2} and is excited to the level $|3\rangle$. Then the three-level system emits a photon of frequency ω_{4+} through the decay channel $|3\rangle \to |1\rangle$. The up conversion efficiency can then be similarly expressed as,

$$\eta_4 = \frac{-\gamma_{31} I_{21}}{2 I_{31}} \frac{(-i\Omega_{32,2})\,\chi_{11}^{(0)}}{V_1 V_2 + \Omega_{32,2}^2}. \tag{B13}$$

3. Output corresponding to frequencies of signal fields

Due to the similar reason as in driving type (1), only attenuation of the probing current can possibly occur in driving type (2). We define as well the gain of the probing current. For the probing current of frequency ω_3, the attenuation rate of the transmitted signal is given by

$$G_3 = 1 + R_3, \tag{B14}$$

with the reflection coefficient

$$R_3 = -\frac{\gamma_{31}}{2} \frac{U_1 \chi_{11}^{(0)}}{U_1 U_2 + \Omega_{32,2}^2}. \tag{B15}$$

Analogously, for the probing current of frequency ω_4, the gain of the transmitted signal is given by

$$G_4 = 1 + R_4. \tag{B16}$$

with the reflection coefficient

$$R_4 = -\frac{\gamma_{21}}{2} \frac{V_1 \chi_{11}^{(0)}}{V_1 V_2 + \Omega_{32,2}^2}. \tag{B17}$$

4. Discussions and numerical calculations

We now summarize the parameters that determine the gains G_k and the conversion efficiencies η_k with $k = 3, 4$. From Eqs. (B14), (B16), (B12), and (B13), we know that G_k and η_k are mainly determined by $\Delta_{32,2}$, $\Omega_{32,2}$ and f, as well as $\delta_{31,3}$ for $k = 3$, and $\delta_{21,4}$ for $k = 4$.

We now study how the extreme values can be obtained by changing the frequency of the signal fields through the probing detunings $\delta_{31,3}$ or $\delta_{21,4}$ with other parameters definite. We know that the extreme values are related to the poles

$$\delta_{31,3}^{(\pm)} = \frac{1}{2}\left(\Delta_{32,2} + i\frac{\Gamma_{21}+\Gamma_{31}}{2}\right) \pm \frac{1}{2}\Delta_{32} \tag{B18}$$

of η_3 (corresponding to the gain G_3) and the poles

$$\delta_{21,4}^{(\pm)} = -\frac{1}{2}\left(\Delta_{32,2} - i\frac{\Gamma_{21}+\Gamma_{31}}{2}\right) \pm \frac{1}{2}\Delta_{32} \tag{B19}$$

of η_4 (corresponding to the gain G_4). Here, the parameter Δ_{32} is defined as $\Delta_{32} = \sqrt{\left[\Delta_{32,2} - i\left(\Gamma_{31}-\Gamma_{21}\right)/2\right]^2 + 4\Omega_{32,2}^2}$. To simplify the discussion, we make the assumption that peaks or dips are well separated from each other, that is, $\sqrt{\Delta_{32,2}^2 + 4\Omega_{32,2}^2} \gg \Gamma_{31}/2, \Gamma_{21}/2$.

a. Frequency conversion, attenuation, and amplification with varying driving detuning

We now study the maximum conversion efficiencies and minimum gains with the conditions

$$\delta_{31,3} = \mathrm{Re}(\delta_{31,3}^{(\pm)}) \tag{B20}$$

for η_3 and G_3, and

$$\delta_{21,4} = \mathrm{Re}(\delta_{21,4}^{(\pm)}) \tag{B21}$$

for η_4 and G_4. Under these conditions, the conversion efficiencies, gains and reflection coefficients are denoted by $\eta_{k\pm}^{\mathrm{I}}$, $G_{k\pm}^{\mathrm{I}}$, and $R_{k\pm}^{\mathrm{I}}$. Let us discuss the gains and the frequency conversions at the point $f = 0.51$ for the bias magnetic flux. In Fig. 11, $|\eta_{k\pm}^{\mathrm{I}}|$ and $|G_{k\pm}^{\mathrm{I}}|$ are plotted as functions of $\Delta_{32,2}/2\pi$ for driving strengths $\Omega_{32,2}/2\pi = 45\,\mathrm{MHz}$ and $\Omega_{32,2}/2\pi = 140\,\mathrm{MHz}$ respectively. And so are $\arg(R_{k\pm}^{\mathrm{I}})$ in Fig. 12. For a given driving strength $\Omega_{32,2}$, the magnitudes of conversion efficiencies η_k^{I} and gains G_k^{I} are determined by the driving detuning $\Delta_{32,2}/2\pi$.

In Figs. 11(a)-(d), the solid and dashed curves plotted according to Eqs. (B20) and (B21) are symmetric about the axis $\Delta_{32,2}/2\pi = 0$. The reasons for these features are similar to those in the driving type (1).

We now investigate the extreme values of $|G_{k\pm}^{\mathrm{I}}|$ and $|\eta_{k\pm}^{\mathrm{I}}|$ corresponding to $\Delta_{32,2}$, through Figs. 11(a)-(d). We find, from Figs. 11(a) and (b), that the local maximum values of $|\eta_{3\pm}^{\mathrm{I}}|$ and $|\eta_{4\pm}^{\mathrm{I}}|$ are about 0.036 and 0.084, respectively. Obviously, the local minimum (maximum) values are namely the minimum (maximum) values. In fact, we have obtained the analytical solution for the optimal driving and probing detuning to obtain the maximum conversion efficiencies. For prob-

ing energy levels $|1\rangle$ and $|3\rangle$, the optimal point is

$$\Delta_{32,2} = \frac{(\Gamma_{31}-\Gamma_{21})}{2}x, \tag{B22}$$

$$\delta_{31,1} = \frac{\Gamma_{31}}{2}x, \tag{B23}$$

$$x = \pm\sqrt{\frac{\Omega_{32,2}^2 - \Gamma_{21}\Gamma_{31}/4}{\Gamma_{21}\Gamma_{31}/4}}, \tag{B24}$$

and the corresponding efficiency is

$$\eta_3 = \frac{-\gamma_{21}I_{31}}{I_{21}}\frac{(-i\Omega_{32,2})}{\Gamma_{21}\Gamma_{31}\,(ix+1)}. \tag{B25}$$

Obviously,

$$|\eta_3| = \left|\frac{\gamma_{21}I_{31}}{2I_{21}}\frac{1}{\sqrt{\Gamma_{21}\Gamma_{31}}}\right|, \tag{B26}$$

which is independent of $\Omega_{32,2}$. For probing energy levels $|1\rangle$ and $|2\rangle$, the optimal point is

$$\Delta_{32,2} = \frac{\Gamma_{31}-\Gamma_{21}}{2}x, \tag{B27}$$

$$\delta_{21,4} = \frac{\Gamma_{21}}{2}x, \tag{B28}$$

and the corresponding efficiency is

$$\eta_4 = \frac{-\gamma_{31}I_{21}}{I_{31}}\frac{(-i\Omega_{32,2})}{\Gamma_{21}\Gamma_{31}\,(ix+1)}. \tag{B29}$$

Obviously,

$$|\eta_4| = \left|\frac{\gamma_{31}I_{21}}{2I_{31}}\frac{1}{\sqrt{\Gamma_{21}\Gamma_{31}}}\right|, \tag{B30}$$

which is also independent of $\Omega_{32,2}$. In Figs. 11(a) and (b), we have labeled those analytical optimal points with "$\circ$"s. We find that the extreme values of $|\eta_{k\pm}^{\rm I}|$ are insensitive to the variation of the driving strength $\Omega_{32,2}$. However, the extreme points will get farther away from the origin as $\Omega_{32,2}$ increases. In Figs. 11(c) and (d), we do not find an extreme value for $|G_{k\pm}^{\rm I}|$, the minimum value occur at the boundaries of the driving detuning $\Delta_{32,2}$. When $\Omega_{32,2} = 45\,\text{MHz}$ and $140\,\text{MHz}$, about 0.66 and 0.69 can be respectively achieved for the minimum $|G_{3\pm}^{\rm I}|$, and about 0.965 and 0.966 can be respectively achieved for the minimum $|G_{4\pm}^{\rm I}|$. Besides, when $\Omega_{32,2}$ increases, achieving the same attenuation of the signal field will require larger detunings.

We now analyze the limitations of $|\eta_{k\pm}|$ and $|G_{k\pm}|$ when $\Delta_{32,2}$ gets larger through examining Figs. 11(a)-(d). Figure 11 shows that when the detuning magnitude $|\Delta_{32,2}| = |\omega_{32}-\omega_{d2}|$ increases, the conversion efficiencies $|\eta_{k\pm}^{\rm I}|$ will approach zero, while the gain $|G_{k\pm}^{\rm I}|$ will approach unity. It is because when the detuning $\Delta_{32,2}$ is large enough, the three-level system will be decoupled from the driving field and thus there is no frequency conversion of the probing fields, which explains why $|\eta_{k\pm}^{\rm I}|$ approach zero. There are different behavior for $|G_{k\pm}^{\rm I}|$ in Fig 11(c) and (d) whether $\Delta_{32,2}$ approaches

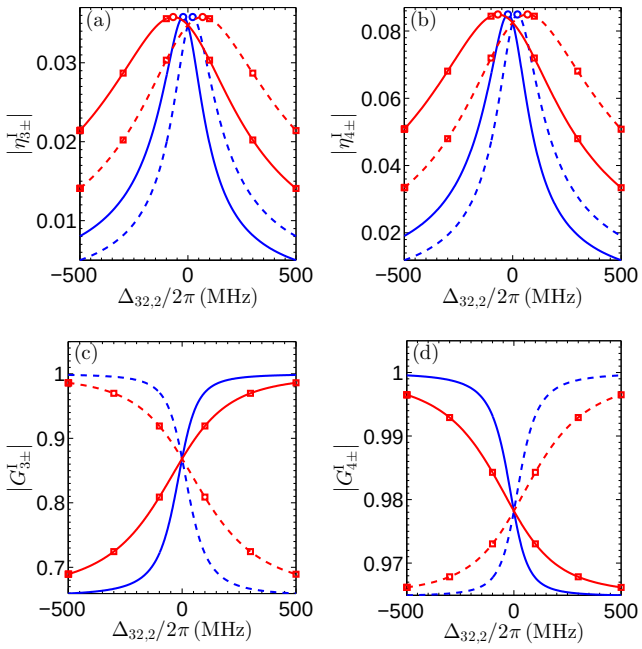

FIG. 11: (Color online) Diving type (2). Conversion efficiency (a) $|\eta_3^{\rm I}|$ and (b) $|\eta_4^{\rm I}|$, and gains (c) $|G_3^{\rm I}|$ and (d) $|G_4^{\rm I}|$ plotted as functions of the driving detuning $\Delta_{32,2}/2\pi$. In all subplots (a)-(d), the blue solid and dashed lines are for the driving strength $\Omega_{32,2}/2\pi = 80\,\text{MHz}$, while the red ones marked with squares are for the driving strength $\Omega_{32,2}/2\pi = 140\,\text{MHz}$. In (a) and (c), the dashed lines are for the probing detuning $\delta_{31,3} = \text{Re}(\delta_{31,3}^{(-)})$ while the solid ones are for the probing detuning $\delta_{31,3} = \text{Re}(\delta_{31,3}^{(+)})$. In (b) and (d), the dashed lines are for the probing detuning $\delta_{21,4} = \text{Re}(\delta_{21,4}^{(-)})$, while the solid ones are for the probing detuning $\delta_{21,4} = \text{Re}(\delta_{21,4}^{(+)})$. The analytical optimal points are marked with circles on the curves for $|\eta_3^{\rm I}|$ and $|\eta_4^{\rm I}|$. The values of other related parameters are taken from Fig. 2 and the reduced bias magnetic flux is taken as $f = 0.51$.

negative infinity or positive infinity. We now explain the reason by taking $|G_{3+}^{\rm I}|$ as an example. When $\Delta_{32,2}$ approaches negative infinity, according to Eq. (B20), the signal field will be resonant to the applied levels, thus undergoing large reflection. Therefore, $|G_{3+}^{\rm I}|$ will approach a non-unity value. However, when $\Delta_{32,2}$ approaches positive infinity, according to Eq. (54), the signal field will be largely detuned from the applied levels, thus undergoing no reflection at all. Therefore, $|G_{3+}^{\rm I}|$ will approach unity.

We now examine $|\eta_{k\pm}^{\rm I}|$ and $|G_{k\pm}^{\rm I}|$ in the resonant driving case through Figs. 11(a)-(d). Specifically, when the driving field is resonantly applied to the three-level system, i.e., $\Delta_{32,2} = \omega_{32}-\omega_{d2} = 0$, we find $|\eta_k^{\rm I}|$ and $|G_k^{\rm I}|$ are also insensitive to the variation of driving strength $\Omega_{32,2}$. But properly detuned driving usually helps achieve better device performance, namely, larger conversion efficiencies and attenuations, than the resonant driving.

In Figs. 12(a)-(b), the solid and dashed curves are symmetric about the origin. The reasons for these features are similar to those in the driving type (1).

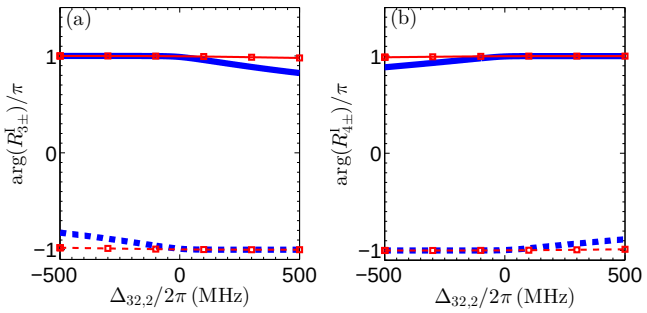

FIG. 12: (Color online) Diving type (2). Phases of the reflection coefficients (a) $|R^{\rm I}_3|$ and (b) $|R^{\rm I}_4|$, plotted as functions of the driving detuning $\Delta_{32,2}/2\pi$. In both subplots (a) and (b), the blue solid and dashed lines are for the driving strength $\Omega_{32,2}/2\pi = 80\,\mathrm{MHz}$, while the red ones marked with squares are for the driving strength $\Omega_{32,2}/2\pi = 140\,\mathrm{MHz}$. In (a), (c), and (e), the dashed lines are for the probing detuning $\delta_{31,3} = \mathrm{Re}(\delta^{(-)}_{31,3})$ while the solid ones are for the probing detuning $\delta_{31,3} = \mathrm{Re}(\delta^{(+)}_{31,3})$. In (b), (d), and (f), the dashed lines are for the probing detuning $\delta_{21,4} = \mathrm{Re}(\delta^{(-)}_{21,4})$, while the solid ones are for the probing detuning $\delta_{21,4} = \mathrm{Re}(\delta^{(+)}_{21,4})$. The analytical optimal points are marked with circles on the curves for $|\eta^{\rm I}_3|$ and $|\eta^{\rm I}_4|$. The values of other related parameters are taken from Fig. 2 and the reduced bias magnetic flux is taken as $f = 0.51$.

We now examine the phases of the reflection coefficients $R_{k\pm}$ through Figs. 12(a) and (b). We find that for the strong driving we have taken, the reflection coefficients have phases of nearly $\pm\pi$. In Figs. 12(a) and (b), the blue solid curves, i.e., the curve for $\arg(R^{\rm I}_{k+})$ when $\Omega_{32,2}/2\pi = 45\,\mathrm{MHz}$, shows a little deviation from $\pm\pi$, when $\delta_{21,4}$ gets larger. But when the driving strength is increased, i.e., $\Omega_{32,2}/2\pi = 140\,\mathrm{MHz}$, the deviation shows significant decrease, as shown by the red solid squared curves. The similar phenomenon also occurs to the dashed lines. By comparison of Fig. 11(c) and Fig. 12(a), or Fig. 11(d) and Fig. 12(b), we find that the smaller one of $|G^{\rm I}_{k+}|$ and $|G^{\rm I}_{k-}|$ always corresponds to a reflection coefficient whose phase is much closer to $\pm\pi$. Guaranteed by Eqs. (B20) and (B21), we can achieve the maximum magnitude of the reflection coefficient. Now the phases $\pm\pi$ of the reflection coefficient are also guaranteed, which makes sure the optimal attenuations are reached.

b. *Frequency conversion, attenuation, and amplification with varying flux bias*

We now study how the conversion efficiencies and the attenuation rates change with the reduced flux bias f. The parameters $\eta^{\rm I}_{k\pm}$, $G^{\rm I}_{k\pm}$, and $R^{\rm I}_{k\pm}$ only depend on the driving detuning $\Delta_{32,2}$, driving strength $\Omega_{32,2}$, and reduced flux bias f. For given $\Omega_{32,2}$ and f, we change the driving detuning $\Delta_{32,2}/2\pi$ from -500 MHz to 500 MHz, and take the optimal $\eta^{\rm I}_{k\pm}$, $G^{\rm I}_{k\pm}$, and $R^{\rm I}_{k\pm}$, which are now denoted by $\eta^{\rm II}_{k\pm}$, $G^{\rm II}_{k\pm}$, and $R^{\rm II}_{k\pm}$, and only depend on $\Omega_{32,2}$ and f. Without loss of generality, we only discuss $\eta^{\rm II}_{k-}$, $G^{\rm II}_{k-}$, and $R^{\rm II}_{k-}$ in the below. The bias dependent $|\eta^{\rm II}_{k-}|$ and $|G^{\rm II}_{k-}|$ have been plotted in Fig. 13, for $\Omega_{32,2}/2\pi = 45$ MHz and $\Omega_{32,2}/2\pi = 140\,\mathrm{MHz}$. And so are $\arg(R^{\rm II}_{k-})$ in Fig. 14.

We now analyze the sensitivity of the conversion efficiencies $|\eta^{\rm II}_{k-}|$ and gains $|G^{\rm II}_{k-}|$ to the variation of the driving strength $\Omega_{32,2}$. For $|\eta^{\rm I}_{k-}|$, the theoretically optimal point can be achieved in the range $-500\,\mathrm{MHz} \le \Delta_{32,2}/2\pi \le 500\,\mathrm{MHz}$, as shown in Figs. 11(a) and (b). Correspondingly, in Figs. 13(a) and (b), we observe an obvious coincidence between the solid blue and dashed red curves, i.e., between the cases $\Omega_{32,2}/2\pi = 45$ MHz and $\Omega_{32,2}/2\pi = 140\,\mathrm{MHz}$. For $|G^{\rm I}_{k-}|$, the theoretically optimal point, which means $\Delta_{32,2}/2\pi$ approaches infinity, can not be achieved in the range $-500\,\mathrm{MHz} \le \Delta_{32,2}/2\pi \le 500\,\mathrm{MHz}$. We see an observable deviation between the solid blue and dashed red curves in Fig. 13(c) and (d).

We now investigate the optimal values for the conversion efficiencies and gains through Figs. 13(a)-(d). We can find that the optimal conversion efficiency $|\eta^{\rm II}_{3-}|$ and $|\eta^{\rm II}_{4-}|$ are respectively about 0.036 and 0.46. The optimal gains $|G^{\rm II}_{3-}|$ and $|G^{\rm II}_{4-}|$ are respectively about 0.66 and 0.08.

We now discuss the behavior at $f = 0.5$ in Fig. 13. When $f = 0.5$, the transition between $|1\rangle$ and $|3\rangle$ is prohibited. Thus no reflection of the signal $\varepsilon_{31,1}$ is induced, i.e., $R^{\rm II}_{3-} = 0$. Due to no reflection, we have $|G^{\rm II}_{3-}| = 1$ at $f = 0.5$, as shown in Fig. 13(c). The frequency conversion process is realized by the cyclic transition. Therefore, the prohibited transition between $|1\rangle$ and $|3\rangle$ induces $|\eta^{\rm II}_3| = |\eta^{\rm II}_4| = 0$ at $f = 0.5$, as shown in Figs. 13(a) and (b). Simultaneously, the prohibited transition makes the populations on level $|2\rangle$ more easily decay to level $|1\rangle$, thus inducing significant reflection of the signal $\tilde{I}_{4p}(0)$. That is why we see a sharp dip in Fig. 13(d).

We now study the phases of the reflection coefficients $R^{\rm II}_{k-}$ through Figs. 14(a) and (b). The phases of both $R^{\rm II}_{3-}$ and $R^{\rm II}_{4-}$ still keep quite close to $\pm\pi$ as the reduced flux bias f changes. This is not surprising since $|G^{\rm II}_{k-}|$ is the optimal $|G^{\rm I}_{k-}|$ with a driving detuning where $|G^{\rm I}_{k-}| < |G^{\rm I}_{k+}|$ must hold. As the preceding discussions on Figs. 12(a) and (b), the smaller one of $|G^{\rm I}_{k-}|$ and $|G^{\rm I}_{k+}|$ usually possesses a reflection coefficient which has a phase much closer to $\pm\pi$. At $f = 0.5$, no reflection of the signal $\varepsilon_{31,3}$ is induced, i.e., $R^{\rm II}_{3-} = 0$, where the mathematically meaningless phase of $R^{\rm II}_{3-}$ is manually set $\arg(R^{\rm II}_{3-}) = 0$. That is why we see a shape peak at $f = 0.5$ in Fig. 14(a).

[1] R. W. Boyd, *Nonlinear Optics* (Academic Press, New York, 2010).

[2] R. L. Abrams, A. Yariv, and P. A. Yeh, IEEE J. Quantum Electron. **QE-13**, 79 (1977); R. L. Abrams, C. K. Asawa, T. K.

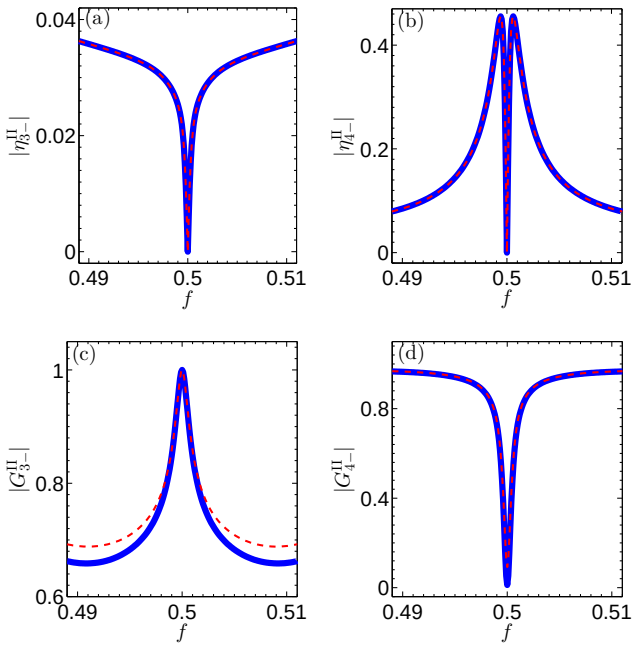

FIG. 13: (Color online) Driving type (2). Conversion frequencies (a) $|\eta_3^{\rm II}|$, and (b) $|\eta_4^{\rm II}|$, and gains (c) $|G_3^{\rm II}|$, (d) $|G_4^{\rm II}|$ plotted as functions of the reduced bias flux f. Here the driving frequency is taken as $\Omega_{32,2}/2\pi = 80\,\mathrm{MHz}$ (blue solid curves) and $\Omega_{32,2}/2\pi = 140\,\mathrm{MHz}$ (red dashed curves). When the reduced bias flux f is permanent and the driving frequency $\Delta_{32,2}$ changes in the range $-500\,\mathrm{MHz} \leq \Delta_{32,2}/2\pi \leq 500\,\mathrm{MHz}$, the values of conversion efficiencies $|\eta_3^{\rm II}|$ and $|\eta_4^{\rm II}|$ and gains $|G_3^{\rm II}|$, and $|G_4^{\rm II}|$ respectively take the maximal values of conversion efficiencies $|\eta_3^{\rm I}|$ and $|\eta_4^{\rm I}|$, and the minimal values of gains $|G_3^{\rm I}|$ and $|G_4^{\rm I}|$.

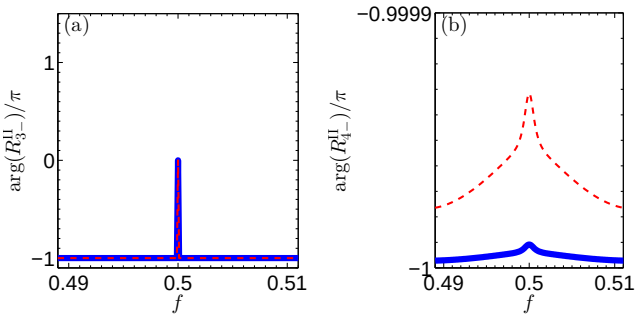

FIG. 14: (Color online) Driving type (2). Phases of the reflection coefficients (a) $\arg(R_{3-}^{\rm II})$ and (b) $\arg(R_{4-}^{\rm II})$ plotted as functions of the reduced bias flux f. Here the driving frequency is taken as $\Omega_{32,2}/2\pi = 80\,\mathrm{MHz}$ (blue solid curves) and $\Omega_{32,2}/2\pi = 140\,\mathrm{MHz}$ (red dashed curves). When the reduced bias flux f is permanent and the driving frequency $\Delta_{32,2}$ changes in the range $-500\,\mathrm{MHz} \leq \Delta_{32,2}/2\pi \leq 500\,\mathrm{MHz}$, the values of conversion efficiencies $|\eta_3^{\rm II}|$ and $|\eta_4^{\rm II}|$ and gains $|G_3^{\rm II}|$, and $|G_4^{\rm II}|$ respectively take the maximal values of conversion efficiencies $|\eta_3^{\rm I}|$ and $|\eta_4^{\rm I}|$, and the minimal values of gains $|G_3^{\rm I}|$ and $|G_4^{\rm I}|$.

Plant, and A. E. Popa, *ibid.* **QE-13**, 82 (1977).

[3] W. Gordy and R. L. Cook, *Microwave Molecular Spectra* (Wiley, New York, 1984).

[4] D. Patterson and J. M. Doyle, Phys. Rev. Lett. **111**, 023008 (2013).

[5] Z. Y. Xue, L. N. Yang, and J. Zhou, Appl. Phys. Lett. **107**, 023102 (2015).

[6] Y. X. Liu, H. C. Sun, Z. H. Peng, A. Miranowicz, J. S. Tsai, and F. Nori, Sci. Rep. **4**, 7289 (2014).

[7] Y. Makhlin, G. Schön, and A. Shnirman, Rev. Mod. Phys. **73**, 357 (2001).

[8] G. Wendin and V. S. Shumeiko, cond-mat/0508729.

[9] J. Clarke and F. K. Wilhelm, Nature (London) **453**, 1031 (2008).

[10] Z. L. Xiang, S. Ashhab, J. Q. You, and F. Nori, Rev. Mod. Phys. **85**, 623 (2013).

[11] J. Q. You and F. Nori, Phys. Today **58**(11), 42 (2005).

[12] J. Q. You and F. Nori, Nature (London) **474**, 589 (2011).

[13] R. J. Schoelkopf and S. M. Girvin, Nature (London) **451**, 664 (2008).

[14] Y. X. Liu, C. P. Sun, and F. Nori, Phys. Rev. A **74**, 052321 (2006).

[15] C. Cohen-Tannoudji, J. Dupont-Roc, and G. Grynberg, *Atom-Photon Interactions: Basic Process and Appilcations* (Wiley-VCH, Weinheim, 1998).

[16] C. M. Wilson, T. Duty, F. Persson, M. Sandberg, G. Johansson, and P. Delsing, Phys. Rev. Lett. **98**, 257003 (2007).

[17] C. M. Wilson, G. Johansson, T. Duty, F. Persson, M. Sandberg, and P. Delsing, Phys. Rev. B **81**, 024520 (2010).

[18] M. Baur, S. Filipp, R. Bianchetti, J. M. Fink, M. Göppl, L. Steffen, P. J. Leek, A. Blais, and A. Wallraff, Phys. Rev. Lett. **102**, 243602 (2009).

[19] M. A. Sillanpää, J. Li, K. Cicak, F. Altomare, J. I. Park, R. W. Simmonds, G. S. Paraoanu, and P. J. Hakonen, Phys. Rev. Lett. **103**, 193601 (2009).

[20] J. Li, G. S. Paraoanu, K. Cicak, F. Altomare, J. I. Park, R. W. Simmonds, M. A. Sillanpää, and P. J. Hakonen, Phys. Rev. B **84**, 104527 (2011); Sci. Rep. **2**, 645 (2012).

[21] A. A. Abdumalikov, Jr., O. Astafiev, A. M. Zagoskin, Yu. A. Pashkin, Y. Nakamura, and J. S. Tsai, Phys. Rev. Lett. **104**, 193601 (2010).

[22] P. M. Anisimov, J. P. Dowling, and B. C. Sanders, Phys. Rev. Lett. **107**, 163604 (2011).

[23] I.-C. Hoi, C. M. Wilson, G. Johansson, J. Lindkvist, B. Peropadre, T. Palomaki, and P. Delsing, New J. Phys. **15**, 025011 (2013).

[24] S. Novikov, J. E. Robinson, Z. K. Keane, B. Suri, F. C. Wellstood, and B. S. Palmer, Phys. Rev. B **88**, 060503(R) (2013).

[25] W. R. Kelly, Z. Dutton, J. Schlafer, B. Mookerji, and T. A. Ohki, J. S. Kline, and D. P. Pappas, Phys. Rev. Lett. **104**, 163601 (2010).

[26] C. P. Yang, S.-I Chu, and S. Han, Phys. Rev. Lett. **92**, 117902(2004).

[27] K. V. R. M. Murali, Z. Dutton, W. D. Oliver, D. S. Crankshaw, and T. P. Orlando, Phys. Rev. Lett. **93**, 087003 (2004).

[28] Z. Dutton, K. V. R. M. Murali, W. D. Oliver, and T. P. Orlando, Phys. Rev. B **73**, 104516 (2006).

[29] H. Ian, Y. X. Liu, and F. Nori, Phys. Rev. A **81**, 063823 (2010).

[30] Hui-Chen Sun, Yu-xi Liu, J. Q. You, E. Il'ichev, and F. Nori, Phys. Rev. A **89**, 063822 (2014). .

[31] Y. X. Liu, J. Q. You, L. F. Wei, C. P. Sun, and F. Nori, Phys. Rev. Lett. **95**, 087001 (2005).

[32] T. P. Orlando, J. E. Mooij, Lin Tian, Caspar H. van der Wal, L. S. Levitov, Seth Lloyd, and J. J. Mazo, Phys. Rev. B **60**, 15398

(1999).
[33] F. Deppe, M. Mariantoni, E. P. Menzel, A. Marx, S. Saito, K. Kakuyanagi, H. Tanaka, T. Meno, K. Semba, H. Takayanagi, E. Solano, and R. Gross, Nature Phys. **4**, 686 (2008).
[34] O. V. Astafiev, A. A. Abdumalikov, Jr., A. M. Zagoskin, Yu. A. Pashkin, Y. Nakamura, and J. S. Tsai, Phys. Rev. Lett. **104**, 183603 (2010).
[35] G. Oelsner, P. Macha, O. V. Astafiev, E. Il'ichev, M. Grajcar, U. Hübner, B. I. Ivanov, P. Neilinger, and H. G. Meyer Phys. Rev. Lett. **110**, 053602 (2013).
[36] S. N. Shevchenko, G. Oelsner, Ya. S. Greenberg, P. Macha, D. S. Karpov, M. Grajcar, U. Hübner, A. N. Omelyanchouk, and E. Il'ichev, Phys. Rev. B **89**, 184504 (2014).
[37] F. Lecocq, I. M. Pop, I. Matei, E. Dumur, A. K. Feofanov, C. Naud, W. Guichard, and O. Buisson, Phys. Rev. Lett. **108**, 107001 (2012).
[38] K. Moon and S. M. Girvin, Phys. Rev. Lett. **95**, 140504 (2005).
[39] N. Roch, E. Flurin, F. Nguyen, P. Morfin, P. Campagne-Ibarcq, M. H. Devoret, and B. Huard, Phys. Rev. Lett. **108**, 147701 (2012).
[40] F. Schackert, A. Roy, M. Hatridge, M. H. Devoret, and A. D. Stone, Phys. Rev. Lett. **111**, 073903 (2013).
[41] M. A. Castellanos-Beltran, K. D. Irwin, G. C. Hilton, L. R. Vale, and K. W. Lehnert, Nat. Phys. **4**, 928 (2008).
[42] T. Yamamoto, K. Inomata, M. Watanabe, K. Matsuba, T. Miyazaki, W. D. Oliver, Y. Nakamura, and J. S. Tsai, Appl. Phys. Lett. **93**, 042510 (2008).
[43] N. Bergeal, F. Schackert, M. Metcalfe, R. Vijay, V. E. Manucharyan, L. Frunzio, D. E. Prober, R. J. Schoelkopf, S. M. Girvin, and M. H. Devoret, Nature **465**, 64 (2010).
[44] N. Bergeal, R. Vijay, V. E. Manucharyan, I. Siddiqi, R. J. Schoelkopf, S. M. Girvin, and M. H. Devoret, Nat. Phys. **6**, 296 (2010).
[45] J. M. Martinis, S. Nam, J. Aumentado, and C. Urbina, Phys. Rev. Lett. **89**, 117901 (2002).
[46] J. Li, G. S. Paraoanu, K. Cicak, F. Altomare, J. I. Park, R. W. Simmonds, M. A. Sillanpää, and P. J. Hakonen, Phys. Rev. B. **84**, 104527 (2011).
[47] J. Li, G. S. Paraoanu, K. Cicak, F. Altomare, J. I. Park, R. W. Simmonds, M. A. Sillanpää, and P. J. Hakonen, (Nature) Sci. Rep. **2**, 645 (2012).
[48] R. Barends, J. Kelly, A. Megrant, D. Sank, E. Jeffrey, Y. Chen, Y. Yin, B. Chiaro, J. Mutus, C. Neill, P. O'Malley, P. Roushan, J. Wenner, T. C. White, A. N. Cleland, and John M. Martinis Phys. Rev. Lett. **111**, 080502 (2013).
[49] M. H. Devoret, in *Quantum Fluctuations (Les Houches Session LXIII)*, edited by S. Reynaud, E. Giacobino, and J. Zinn-Justin (Elsevier, 1997), pp. 351.
[50] B. Yurke and J. S. Denker, Phys. Rev. A **29**, 1419 (1984).
[51] C. Gardiner and M. Collett, Phys. Rev. A **31**, 3761 (1985).
[52] C. Gardiner and P. Zoller, *Quantum Noise: a Handbook of Markovian and Non-Markovian Quantum Stochastic Methods with Applications to Quantum Optics* (Springer, Berlin, 2000), Vol. **56**.
[53] D. F. Walls and G. G. J. Milburn, *Quantum Optics* (Springer, Berlin, 2008).
[54] C. Gardiner, A. Parkins, and P. Zoller, Phys. Rev. A **46**, 4363 (1992).
[55] J. Gough and M. R. James, Automatic Control, IEEE Transactions on **54**, 2530 (2009).
[56] O. Astafiev, A. M. Zagoskin, A. Abdumalikov, Y. A. Pashkin, T. Yamamoto, K. Inomata, Y. Nakamura, and J. Tsai, Science **327**, 840 (2010).
[57] O. Astafiev, A. Abdumalikov Jr, A. M. Zagoskin, Y. A. Pashkin, Y. Nakamura, and J. Tsai, Phys. Rev. Lett. **104**, 183603 (2010).
[58] A. A. Abdumalikov Jr, O. Astafiev, Y. Nakamura, Y. A. Pashkin, and J. Tsai, Phys. Rev. B **78**, 180502 (2008).
[59] J. Koch, T. M. Yu, J. Gambetta, A. A. Houck, D. I. Schuster, J. Majer, A. Blais, M. H. Devoret, S. M. Girvin, and R. J. Schoelkopf, Phys. Rev. A **76**, 042319 (2007).
[60] A. A. Houck, J. A. Schreier, B. R. Johnson, J. M. Chow, J. Koch, J. M. Gambetta, D. I. Schuster, L. Frunzio, M. H. Devoret, S. M. Girvin, and R. J. Schoelkopf, Phys. Rev. Lett. **101**, 080502 (2008).